nature biomedical engineering

Article

https://doi.org/10.1038/s41551-023-01137-8

Assessment of visual function in blind mice and monkeys with subretinally implanted nanowire arrays as artificial photoreceptors

Received: 15 January 2022

Accepted: 17 October 2023

Published online: 23 November 2023

Check for updates

Ruyi Yang[1,12], Peng Zhao[1,12], Liyang Wang[2,12], Chenli Feng[2,12], Chen Peng[3,12], Zhexuan Wang[1], Yingying Zhang[4], Minqian Shen[2], Kaiwen Shi[1], Shijun Weng[1], Chunqiong Dong[2], Fu Zeng[4], Tianyun Zhang[1], Xingdong Chen[1], Shuiyuan Wang[5], Yiheng Wang[1], Yuanyuan Luo[1], Qingyuan Chen[1], Yuqing Chen[1], Chengyong Jiang[1], Shanshan Jia[6], Zhaofei Yu[6], Jian Liu[7], Fei Wang[8], Su Jiang[8], Wendong Xu[8,9], Liang Li[10], Gang Wang[10], Xiaofen Mo[1], Gengfeng Zheng[3], Aihua Chen[4], Xingtao Zhou[1], Chunhui Jiang[1] ✉, Yuanzhi Yuan[2,11] ✉, Biao Yan[1] ✉ & Jiayi Zhang[1] ✉

Retinal prostheses could restore image-forming vision in conditions of photoreceptor degeneration. However, contrast sensitivity and visual acuity are often insufficient. Here we report the performance, in mice and monkeys with induced photoreceptor degeneration, of subretinally implanted gold-nanoparticle-coated titania nanowire arrays providing a spatial resolution of 77.5 μm and a temporal resolution of 3.92 Hz in ex vivo retinas (as determined by patch-clamp recording of retinal ganglion cells). In blind mice, the arrays allowed for the detection of drifting gratings and flashing objects at light-intensity thresholds of 15.70–18.09 μW mm^{-2}, and offered visual acuities of 0.3–0.4 cycles per degree, as determined by recordings of visually evoked potentials and optomotor-response tests. In monkeys, the arrays were stable for 54 weeks, allowed for the detection of a 10-μW mm^{-2} beam of light (0.5° in beam angle) in visually guided saccade experiments, and induced plastic changes in the primary visual cortex, as indicated by long-term in vivo calcium imaging. Nanomaterials as artificial photoreceptors may ameliorate visual deficits in patients with photoreceptor degeneration.

Photoreceptor degeneration caused by retinitis pigmentosa (RP) or age-related macular degeneration (AMD) has long been a major cause of blindness. Despite the loss of photoreceptors in the retina, the remaining retinal cells as well as their projections to the brain are preserved from the disease. In the past decade, success in treating Leber congenital amaurosis (LCA) using adeno-associated virus (AAV)-based treatment has opened up opportunities in gene therapy[1,2]. Recent studies using genetic and stem-cell-based strategies have made progress in providing proof-of-principle evidence of restoring light sensitivity in photoreceptor-degenerated mice[3–7]. One clinical study showed that, with the help of engineered goggles, a patient with RP exhibited partial restoration of vision with retinal expression of optogenetic proteins[8]. Yet there are challenges in the restoration of image-forming vision with high sensitivity, as well as biosafety issues[9].

The multielectrode stimulation devices turn light signals in the external world into patterned electrical currents and stimulate the

A full list of affiliations appears at the end of the paper. ✉e-mail: chhjiang70@163.com; yuan.yuanzhi@zs-hospital.sh.cn; biaoyan@fudan.edu.cn; jiayizhang@fudan.edu.cn

remaining retinal cells to establish visual perception in blind patients with late-stage photoreceptor-degenerating diseases[10]. Argus II, a device with 60 pixels, received market approval in both Europe and the United States. The epiretinal implant of Argus II enabled blind patients to not only perceive light but also perform certain visual tasks[11–13], despite issues of limited visual acuity and safety profile in multicentre studies[14]. Similar issues occurred to subretinal implant Alpha AMS[15,16]. Both Argus II and Alpha AMS were discontinued, despite the market authorization they had. These early efforts in retinal prosthesis were followed by subretinal implant PRIMA with 378-pixel electrical stimulation (each pixel is 100 μm in diameter) in the retina of human patients[17,18]. For experiments of retina in pigmented rat[19], retinal responses to prosthetic stimulation exhibit flicker fusion at high frequencies. For prosthetic vision with 40-μm and 20-μm implants[20], the spatial resolution was 34.3 μm and 27.5 μm with alternating gratings (near-infrared stimulus, 1.2 mW mm^{-2}) in ex vivo experiments, reaching the 28-μm limit of the natural visual resolution in rats. The stimulation thresholds for full-filed activation in visually evoked potentials (VEPs) recording was 0.06 mW mm^{-2} with 10-ms pulse[20,21]. The stimulation thresholds were 6.7 ms for 0.58 mW mm^{-2} irradiance in RCS rats with PRIMA implant[22]. Three non-human primates recovered saccade with stimulations at the implant regions with 200 μW mm^{-2} near-infrared light[23]. With the assistance of video glasses that turns visible light into pulsed near-infrared light, patients achieved better visual acuity than those implanted with Argus II (ref. 17). A neuroprosthesis with multichannel electrical stimulation implanted intracranially into V1 also enabled vision in monkeys and humans[24,25], despite the more invasive surgical procedure compared with retinal prosthesis. Organic photovoltaic and injectable nanoparticles provided proof-of-principle evidence for light perception in blind mice and shed light onto the next generation of retinal prosthesis with improved surgical procedure and spatial resolution[26–29].

We previously developed Au-nanoparticle-decorated titania nanowire arrays (Au–TiO_2 NW arrays), in which each NW was roughly 100 nm in diameter and 2 μm in length, with a similar physical size to photoreceptors. NW arrays converts ultraviolet (UV), blue and green light into photocurrent to activate retinal ganglion cells (RGCs) in retinal degenerated 1 knockout/cone diphtheria toxin subunit-A (*rd1/cDTA*) blind mice, with light intensity threshold as low as 10 μW mm^{-2} and a spatial resolution of 100 μm ex vivo[30]. The performance of the NW arrays in restoring primary visual functions in vivo is yet to be evaluated. In this Article, we developed $AuTiO_{2-x}$ NW arrays (which we will refer to simply as 'NW array') with an enhanced UV–visible photocurrent (5–7 times) compared with Au–TiO_2 NW arrays that were previously published[30].

One important issue in retinal prosthesis is the spatial and temporal resolutions in restored vision. Under the stimulation intensity of 80 μW mm^{-2}, the NW-array-attached retina responded to 0.5–20 Hz flickering stimuli ex vivo, and the NW-array-implanted blind mice responded to 1.4–17° gratings. NW-implanted blind mice had a visual acuity of 0.3 cycles per degree (c.p.d.) in optomotor test and recognized static, moving and flashing objects, and discriminated horizontal gratings from vertical gratings in the choice-box behaviour experiments, respectively. These evidence collectively indicate that implantation of NW arrays caused significant improvements in temporal and spatial resolution in blind mice. Finally, we implanted NW arrays into the subretinal space of monkeys and showed good biocompatibility up to 54 weeks. Visually guided saccade (VGS) to the NW-implanted area suggested the perception of a light-emitting diode (LED) of 0.5° in beam angle at 10 μW mm^{-2}.

Results

Enhanced photocurrent of $AuTiO_{2-x}$ NW arrays

Compared with our previous study[30], we conducted an additional step of thermal annealing in H_2/Ar after hydrothermal growth, to create oxygen vacancies and prepare TiO_{2-x} NW arrays. Au nanoparticles were then in situ reduced and deposited on the NW arrays surface to obtained $AuTiO_{2-x}$ NW arrays. The X-ray diffraction (XRD, Supplementary Fig. 1a) pattern presented two peaks at 36.3° and 63.1° that matched well with rutile TiO_2 (101) and (002) planes. The NW arrays were composed of highly dense single NW with average lengths of 2.5 μm and average diameters of 100 nm (Supplementary Fig. 1b,c). High-resolution transmission electron microscopy images showed that the lattice spacing of the dark nanoparticles and NW arrays were 0.235 and 0.246 nm (Supplementary Fig. 1c and inset), corresponding to cubic-phase Au (111) planes (JCPDS# 00-001-1172) and rutile-phase TiO_2 (101) planes (JCPDS# 01-088-1175), respectively. The spherical aberration-corrected high-angle annular dark-field scanning transmission electron microscopy image (Supplementary Fig. 1d) showed the array of bright Ti (highlighted by blue spheres) and dark O (highlighted by red spheres) contrast on rutile TiO_2 (101) planes. The extracted intensity from the yellow dashed line of the fourth O atom greatly decreased (Supplementary Fig. 1e), indicating the oxygen vacancies[31]. The existence of oxygen vacancies was further confirmed by X-ray photoelectron spectroscopy (Supplementary Fig. 1f), in which the modified $AuTiO_{2-x}$ presented an additional shoulder peak centred at about 532.5 eV (ref. 32).

When illuminated by UV (375/28 nm, 292.99 μW mm^{-2}), blue (470/20 nm, 318.47 μW mm^{-2}), green (546/12 nm, 420.38 μW mm^{-2}) or red (697/30 nm, 331.21 μW mm^{-2}) light, the average photocurrents of the newly fabricated NW arrays were about 13,000, 1,300, 1,100 and 30 pA, respectively (Extended Data Fig. 1a,b), which was consistent with its adsorption spectrum (Extended Data Fig. 1c). The photocurrents under UV, blue and green light increased by five to seven times compared with those reported in our previous study[30] (Extended Data Fig. 1d).

The photocurrent of NW arrays was composed of two phases: capacitive and faradaic (Extended Data Fig. 1e–h). In the following measurement, the amplitude of photocurrent refers to that of the capacitive current. When illuminated by UV light, the mean amplitude of capacitive photocurrents in NW arrays were 5,876 pA at 10 μW mm^{-2} and 3,153 pA and 3 μW mm^{-2}, respectively (Extended Data Fig. 1e,f). Amplitude of capacitive photocurrent remained constant at durations of 0.005–1 s (Extended Data Fig. 1g). The mean latency (time to

Fig. 1 | Ex vivo responses of RGCs to light stimulus, and in vivo light localization test. a, Schematic of patch-clamp recording of RGCs in blind mice with NW arrays attached. **b**, Fraction of response of RGCs in blind retinas with NW arrays or glass attached with different pulse durations. Dashed green line indicated the stimulation threshold (50% fraction of responses). Dashed red lines indicated the pulse duration corresponding to the stimulation threshold. n = 30 RGCs from 9 retinas for blind with NW arrays. n = 8 RGCs from 4 retinas for blind with glass. **c**,**d**, Analysis of responses of RGCs in blind retina with NW arrays or glass. n = 14 RGCs from 6 retinas for blind with NW arrays. n = 11 RGCs from 6 retinas for blind with glass. Fraction of response in 30 trials (**c**) and normalized cell responses (**d**). **e**, Responses of a representative RGC in NW-array-attached blind retina to stimulus (1 s duration, 10 s interval) with different light intensities. **f**,**g**, Schematics and behavioural paradigm for choice-box-based behavioural test. **h**, Schematics of light localization test. **i**, Correct rate of normal mice (n = 6 mice), blind mice with glass implant (n = 6 mice) and blind mice with NW array implant (n = 8 mice). **j**,**k**, Correct rate of light localization test using blue and green LEDs with different light intensities. **l**, Timeline of light localization test in 1-week group and 4-week group mice. **m**, Number of testing days when the correct rate reached 70% and maintained steady for 3 days of normal mice (n = 3 mice for each group) and blind mice with NW array implant in 1-week and 4-week group (n = 4 mice for each group) in the choice-box-based behavioural test. All data are expressed as mean ± SEM. Statistical significance was determined using one-way ANOVA with Tukey's multiple comparisons in **i**, **j**, **k** and **m**. Asterisk indicates a significant difference between blind mice with NW arrays and blind mice with glass implant; '#' indicates a significant difference between blind mice with NW arrays and normal mice. ** and ##, P < 0.01; *** and ###, P < 0.001.

https://doi.org/10.1038/s41551-023-01137-8

capacitive peak from the onset of stimuli) of $AuTiO_{2-x}$ NW arrays was 0.26 ms (Extended Data Fig. 1i,j). Faradaic phase lasts until the end of stimulus (Extended Data Fig. 1i).

We used *rd1/cDTA* mice (referred to as blind mice below), in which photoreceptors were completely degenerated by P50 (referred to as blind mice, Supplementary Fig. 2a–c). In blind retina with NW arrays

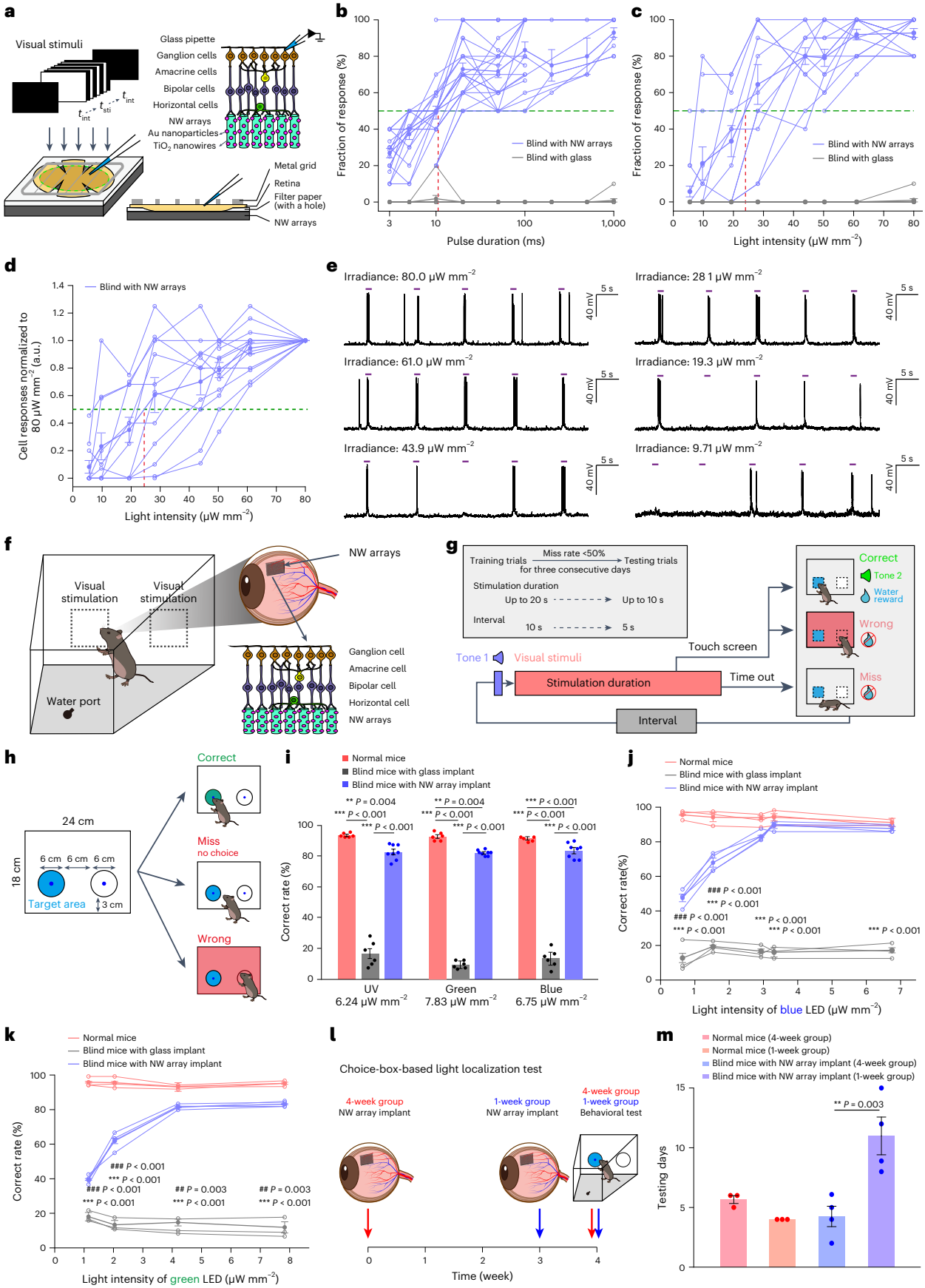

https://doi.org/10.1038/s41551-023-01137-8

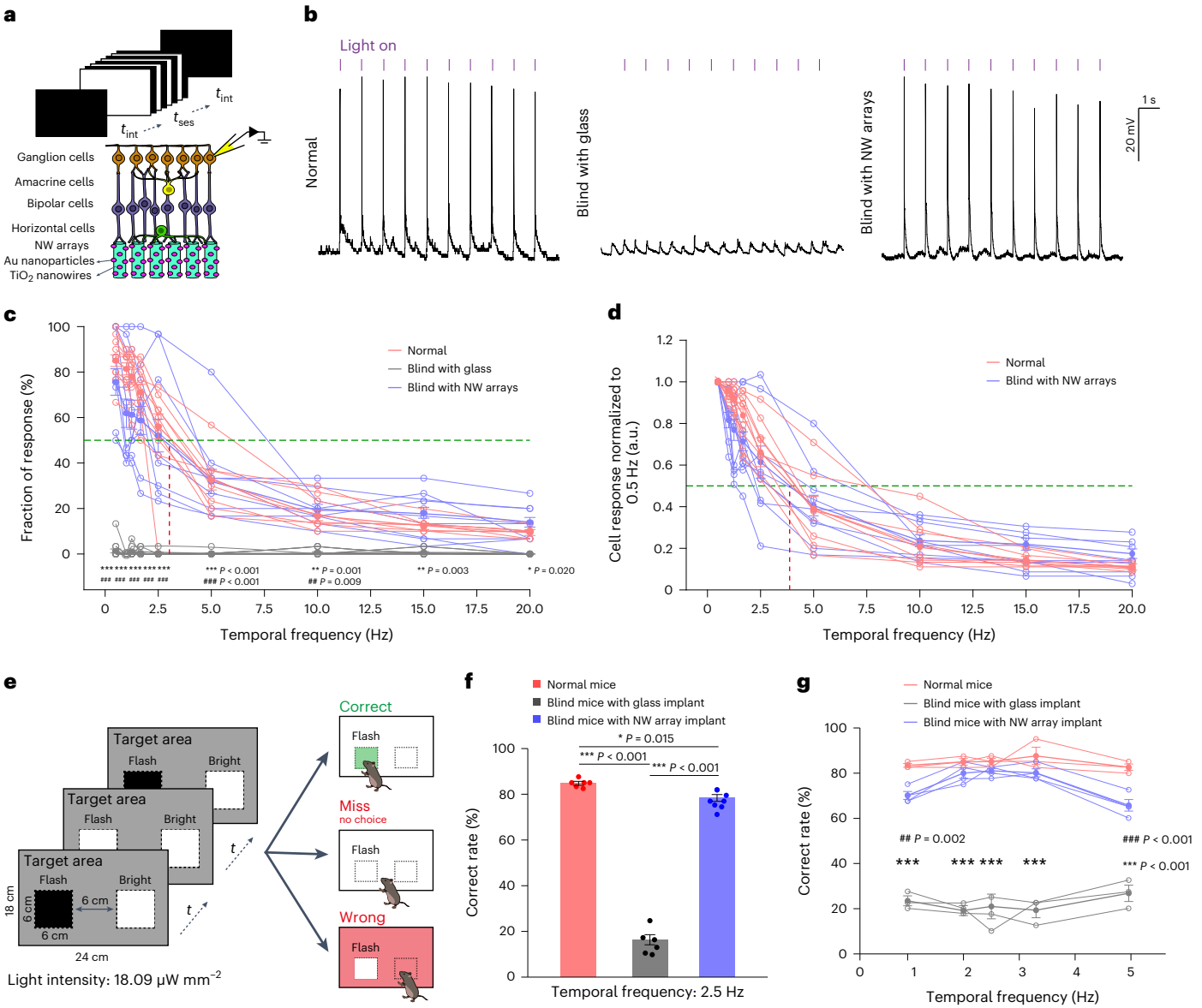

Fig. 2 | Ex vivo responses of RGCs to flashing light, and in vivo flashing detection test. a, Schematic of ex vivo patch-clamp recording under flash stimuli at different stimulation rates. **b**, Responses of representative RGCs from normal retina, blind retina with glass and blind retina with NW arrays attached to flash stimuli (duration 25 ms, frequency 1.0 Hz). **c**,**d**, Analysis of responses of RGCs. Normal: $n = 12$ RGCs from 3 retinas. Blind with glass: $n = 15$ RGCs from 3 retinas. Blind with NW arrays: $n = 16$ RGCs from 4 retinas. Fraction of response (**c**) and normalized cell responses (**d**). $^{*}P < 0.05$, $^{**}P < 0.01$, $^{***}P < 0.001$ blind with NW arrays versus blind with glass. $\#\#\ P < 0.01$, $\#\#\#\ P < 0.001$ normal versus blind with glass. **e**, Schematics of flashing detection test. *t* indicates the duration of stimuli, which was equal to the interval of stimuli. **f**, Correct rates of flashing detection test with temporal frequency at 2.5 Hz ($t = 0.2$ s). Normal mice: $n = 6$ mice. Blind mice with glass implant: $n = 6$ mice. Blind with NW array implant: $n = 8$ mice. $^{*}P < 0.05$, $^{***}P < 0.001$. **g**, Correct rate of flashing detection test with different temporal frequency (1.0–5.0 Hz). Normal mice: $n = 3$ mice. Blind mice with glass implant: $n = 3$ mice. Blind with NW array implant: $n = 4$ mice. $^{***}P < 0.001$ blind mice with NW array implant versus blind mice with glass implant. $\#\#\ P < 0.01$, $\#\#\#\ P < 0.001$ normal mice versus blind mice with NW array implant. All data are expressed as mean ± s.e.m. Statistical significance was determined using one-way ANOVA with Tukey's multiple comparisons in **f**, and two-way RM ANOVA with Tukey's multiple comparisons in **c** and **g**.

attached, the percentage of responsive RGCs was 97.12% (Supplementary Fig. 3a,b). Similar to our previous work[30], 36.3% of RGCs in blind retina with NW arrays attached showed sustained On response (S-RGCs), whereas 63.7% of RGCs showed transient On responses (T-RGCs) (Supplementary Fig. 3b,c). The mean latency of T-RGCs and S-RGCs in normal retina were significantly larger than that in blind retina with NW arrays attached (Supplementary Fig. 3d). However, the durations of response in blind retina with NW arrays attached were similar to that in normal retina (Supplementary Fig. 3e). Furthermore, T-RGCs and S-RGCs exhibited consistent transient and sustained responses when the duration of the stimulus was reduced to 500, 100 and 25 ms (Supplementary Fig. 3f). When NW arrays were attached to the blind retina, the RGCs of blind mice were activated by UV, blue or green light, respectively (Supplementary Fig. 3g).

To estimate the safety profiles in our system, UV light stimuli (digital micromirror device (DMD), wavelength 400 nm, intensity 80 μW mm^{-2}) with various pulse durations (0.003–1.0 s) were applied to blind retina with NW arrays attached (Fig. 1a). We provided 30 stimulations (trials) in total for each cell and divided these 30 stimulations into 3 sessions (10 stimulations in each session) with 10-s intervals

https://doi.org/10.1038/s41551-023-01137-8

in between (Supplementary Fig. 4). A trial was defined as responsive when action potentials were elicited during stimulation. Fraction of response was calculated by the number of responsive trials divided by total number of trials (30 light pulses), which increased with the elongation of pulse duration (Fig. 1b and Supplementary Fig. 5). Stimulation threshold was defined as the pulse duration at which fraction of response is 50%, which was 13.984 ms for NW-array-attached blind retina at 80 μW mm^{-2}. One-second light pulse at different light intensities (5–80 μW mm^{-2}) were presented to NW-array-attached blind retina to investigate whether the RGC responses could be modulated by light. The fraction of NW-array-mediated light responses and normalized cellular responses decreased with decreasing light intensities (Fig. 1c–e), reaching 50% (fraction of response) when light intensity was 24.01 μW mm^{-2}.

Light-source identification in blind mice implanted with the NW arrays

To further explore whether the NW-array-implanted blind mice exhibit light perception behaviour, we modified the protocols of choice-box-based two-alternative forced choice (2AFC) task[33]. In our choice-box experiments, visual stimuli were delivered as they would naturally occur under natural circumstances. Two visual stimuli were projected onto one side of a rectangular box, and the opposite side was installed with one water port (Fig. 1f). The behavioural experiments consisted of training and testing trials (Fig. 1g). The purpose of the training trials was for the mice to learn the association between touching the screen and getting the water reward, whereas the purpose of the testing trials following training trials was to test whether the mice was capable of locating the light source. During the training trials, 2–3 s after tone 1 (a preparation cue), visual stimuli were presented for 20 s with stable light intensity (or until the termination of the trials, defined as stimulation duration). If the mice touched the target area (Fig. 1g,h), tone 2 (a cue for water reward) was provided and the mice received a water reward. If mice did not touch the screen (miss) or touched areas outside the target area (wrong), they would not get a water reward. The miss trial is designed to terminate the trial if the animal (blind mice in particular) could not perceive light or learn to touch the screen during stimulation duration. When the miss rate (percentage of 'miss' trials across all trials) of normal mice was less than 50% for more than three consecutive days in training trials (Extended Data Fig. 2a), the behaviour paradigm of all mice was switched to testing trials. All mice used in our behavioural experiments entered testing trials.

In the testing trials, a correct trial was defined when the mice touched the target area corresponding to the pre-selected visual stimulus (defined in each of the following experiments). We reduced the stimulation duration from 20 s to 10 s so that the normal and NW-array-implanted blind mice were instructed to spend less time touching the wrong places on the screen and pay attention to the visual stimuli to get water reward. The normal and NW-array-implanted blind mice learnt to locate the water port and drinking water within a few seconds towards the end of the training trials; hence, we reduced intervals from 10 s in training trials to 5 s in testing trials, similar to the 8-s interval in a previous study[33].

We implanted NW arrays subretinally into blind mice as previously shown[30] and used UV, blue and green LEDs to test whether the mice could recognize the locations of LEDs (Fig. 1h). All mice used were over postnatal day 90, and the blind mice were implanted with NW arrays or glass for over 1 month (Supplementary Table 1). In each trial, one of the two LEDs were turned on. If mice touched the target area (6 cm in diameter centred at the on-LED) corresponding to the ON LED, they received a water reward (correct trial) (Supplementary Video 1). The correct rates (correct trials divided by all trials) of normal mice were 94.17%, 95% and 91.11%, for UV, green and blue LEDs, respectively, whereas that for blind mice implanted with glass were less than 25% for all three colours. For blind mice with NW array implant, the correct rate was 82.71%, 82.29% and 83.85% for UV, green and blue light, respectively (Fig. 1i). There was no significant difference in the correct rate between NW-array-implanted mice and normal mice when light intensities were above 3.31 μW mm^{-2} for blue light and 6.75 μW mm^{-2} for green light (Fig. 1j,k).

We also conducted light localization test using 25-ms pulses at 20 Hz as well as static objects in separate experiments. The correct rates for detecting 20 Hz flashing light were 85.20%, 15.68% and 82.07%, for normal mice, blind mice with glass implant and blind mice with NW array implant, respectively (Extended Data Fig. 2b, c). In static object recognition test, the mice were trained to touch the static object which appears at random positions in the choice box (Extended Data Fig. 3a and Supplementary Video 2). The correct rate of normal mice and blind mice with NW array implant were 90% and 86%, respectively (Extended Data Fig. 3b).

To investigate whether the duration of NW array implants affects the behavioural performance, we conducted light-source localization experiments in two groups of NW-array-implanted mice: one group implanted with NW arrays for 4 weeks and the other group implanted with NW arrays for 1 week (Fig. 1l). Neither 4-week nor 1-week groups went through any behavioural training before the light-source localization test. In the 4-week group, NW-array-implanted blind mice had a similar correct rate to that for normal mice from testing day 1 to day 9 (Extended Data Fig. 3c). However, in the 1-week group, the correct rate for NW-array-implanted blind mice was significantly smaller than that for normal mice. Interestingly, it took the 4-week group 4.25 testing days to reach a correct rate of 70% on three consecutive days, shorter than 10.99 testing days in the 1-week group (Fig. 1m). These results indicated that NW-array-implanted mice in the 4-week group were better at localizing the LED than the 1-week group.

Perception of flashing light in blind mice implanted with the NW arrays

We first measured photocurrents from $AuTiO_{2-x}$ NW arrays in response to flashing light (0.5–60 Hz, 50% duty cycle, 400 nm, 10 μW mm^{-2}) to investigate the temporal response properties of the device. Photocurrent was reliably elicited by every stimulus for up to 60 Hz (Supplementary Fig. 6a). The amplitude of the photocurrent remained steady for

Fig. 3 | Spatial resolution and receptive field in blind mice with the implanted NW arrays. a, Schematic of ex vivo patch-clamp recording with grating stimuli. **b**, Responses of representative RGCs from normal retinas, glass-attached and NW-array-attached blind retinas to alternating gratings. Light was pulsed at 4 Hz and the grating contrast reversed at 1 Hz (contrast reversal every 500 ms). **c**, Fraction of responses of RGCs. Normal: $n = 13$ RGCs from 4 retinas. Blind with glass: $n = 10$ RGCs from 3 retinas. Blind with NW arrays: $n = 18$ RGCs from 5 retinas. **d**, Histograms and kernel density estimates of the stimulation thresholds distributions in **c**. **e**, Schematic of VEP recordings. **f**, Sample VEP traces of blind mice with NW array implant. The VEP amplitude was defined as the peak-to-peak variation of the signal during the first 300 ms following grating alternation (purple shaded area). **g**, VEP amplitude for alternating gratings in normal mice (red: $n = 5$ mice) and blind mice with NW array implant (blue: $n = 4$ mice). **h**, Schematics of the optomotor test. **i**,**j**, Contrast sensitivity (**i**) and visual acuity (**j**) of normal mice ($n = 5$ mice), blind mice with glass implant ($n = 3$ mice) and blind mice with NW array implant ($n = 4$ mice). **k**, Schematics of receptive field (RF) mapping. **l**, GCaMP6s fluorescence signals from representative V1 neurons in normal mice and blind mice with NW array implant in response to one visual stimulus (individual trace in grey, average in black) ordered according to stimulus position. Red circles indicate the outline of calculated receptive field. **m**, Heatmap of average responses in **l**. **n**,**o**, Distribution (**n**) and mean areas (**o**) of receptive fields of normal mice ($n = 99$ cells from 4 mice) and blind mice with NW array implant ($n = 13$ cells from 3 mice). All data are expressed as mean ± s.e.m. Statistical significance was determined using one-way ANOVA with Tukey's multiple comparisons in **j**, two-sided unpaired *t*-test in o. NS, non-significant; $^{**}P < 0.01$, $^{***}P < 0.001$.

https://doi.org/10.1038/s41551-023-01137-8

1,000 repetitive stimuli at 1 Hz, 10 Hz and 20 Hz (Supplementary Fig. 6b, average of the last ten pulses/first response was 90.72% at 1 Hz, 88.89% at 10 Hz, and 86.25% at 20 Hz). Upon 30 min stimulation at 20 Hz (pulse duration 25 ms, 10 μW mm^{-2}, 36,000 stimuli), the average amplitude of the photocurrent for the last 100 pulses was 84.30% of the very first pulse (Supplementary Fig. 6c).

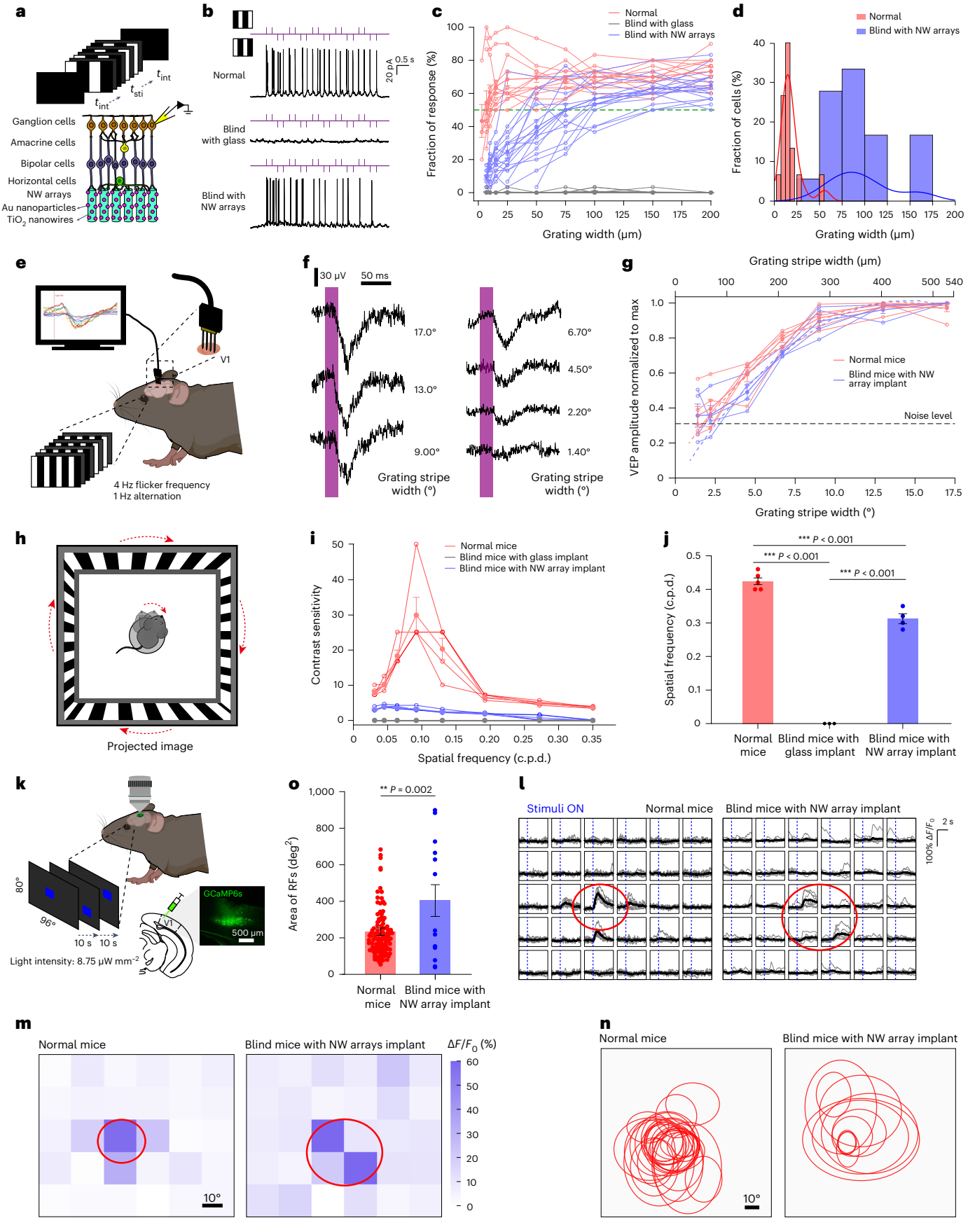

https://doi.org/10.1038/s41551-023-01137-8

Based on the good temporal profile in NW arrays, we examined the temporal resolution in RGCs of blind mouse retina attached to NW arrays (Fig. 2a,b). Inspired by the PRIMA study in RCS rat[19], 0.5–20 Hz pulsed full-field illumination (400 nm, 80 μW mm^{-2}, pulse duration 25 ms) was presented to blind retina with NW arrays attached. Each cell was provided a total of 30 stimulations (trials) as in the experiment testing the stimulation threshold (Supplementary Fig. 4). The fraction of response was calculated as the number of responsive trials divided by total number of trials (30). In both NW-array-attached blind retinas and normal retinas, fraction of responses and response normalized to 0.5 Hz decreased with the increasing temporal frequency (Fig. 2c,d). The threshold of temporal resolution was defined as the flicker frequency that resulted in a 50% probability of eliciting an action potential. In the normalized cell response of RGCs (UV light stimulus: 400 nm, 80 μW mm^{-2}) to different frequency stimuli, the threshold of RGCs in normal retina and NW-array-attached blind retina was 4.01 and 3.92 Hz, respectively (Fig. 2d). We used stimuli with a temporal frequency of 4 Hz (an integer closest to 3.92 Hz) for convenience in subsequent ex vivo patch-clamp recording and in vivo VEP recording experiments. When the flashing frequencies were above 2.5 Hz, RGCs in both normal retina (Extended Data Fig. 4a,b) and NW-array-attached blind retina (Supplementary Fig. 7a,b) responded at the beginning of the stimulation, but failed to evoke action potentials in every remaining pulse.

In addition, under the current test conditions, the safety thresholds calculated according to Rule 2 and Rule 3 of the ANSI 2000 standard[34] were 31.91 μW and 87.54 μW, respectively, which were larger than the radiation power of stimulus used in our electrophysiological experiments (for further details, see Methods). Meanwhile, with a fixed single pulse duration of 25 ms and 20 s exposure duration, the maximum acceptable pulse rate for safety was 40 Hz (for further details, see Methods).

To evaluate the temporal resolution of NW arrays in vivo, NW-array-implanted mice were trained to touch the target area associated with flashing light (Fig. 2e, Extended Data Fig. 3d and Supplementary Video 3). All mice were over postnatal day 240 and implanted with NW arrays or glass for over 6 months, which were earlier tested in the light localization test and moving bar detection test (details in Methods and Supplementary Table 1). The correct rates of normal mice and blind mice with NW array implant were 84.80% and 78.39%, respectively, whereas the correct rate for blind mice with glass implant was 16.37% (Fig. 2f,g). When the frequency of flash stimulation was either larger than 5 Hz or smaller than 1 Hz, the correct rate of NW-array-implanted blind mice was slightly smaller than that of normal mice, but still significantly higher than that of blind mice (Fig. 2g).

Spatial resolution in blind mice implanted with the NW arrays

Spatial resolution affects one of the most important features of vision: visual acuity[35], which is associated with the ability to resolve details and critical to pattern recognition[36]. Inspired by previous PRIMA study in rats[19], alternating gratings stimuli were presented in NW-array-attached blind retina to assess the spatial resolution in ex vivo experiments. Stimuli were presented by DMD (400 nm, 80 μW mm^{-2}) with 25 ms pulsed duration at 4 Hz flicker frequency (an integer closest to 3.92 Hz temporal frequency) and 1 Hz grating alternation (Fig. 3a). The width of the square-wave grating stripes varied from 3 μm to 200 μm. The fraction of response in RGCs increased with increasing widths of the grating in both normal retina and NW-array-attached blind retina (Fig. 3b and Supplementary Fig. 7c,d). We also defined the stimulation threshold as the grating stripe size that resulted in a 50% probability of eliciting an action potential correlated with the grating contrast reversal, which was around 74.8 μm in blind retina with NW arrays attached and 5.5 μm in normal retina (Fig. 3c). The distribution of thresholds measured peaked at 14.90 μm in normal retina and at 84.75 μm in blind retina with NW arrays attached (Fig. 3d).

Recording VEPs with alternating gratings are also a well-established in vivo method for assessing spatial resolution in animals[19]. We recorded VEPs in the visual cortex induced by alternating gratings (DMD, 400 nm, 80 μW mm^{-2}) with different widths (3–200 μm, Fig. 3e). The VEP amplitude was calculated as the difference between the maximum and minimum of the cortical signal during the first 300 ms period post stimulus. As shown in Fig. 3f,g, the VEP amplitude decreased with increasing spatial frequency for both normal mice and blind mice with NW array implant. Inspired by previous PRIMA study[22], acuity limit was defined as the intersection of the fitting line in the response curve with the noise level (dashed lines in Fig. 3g). For blind mice with NW array implant, the acuity limit was 2.50° (77.50 μm on retina, 1° corresponds to 31 μm on mouse retina[37]), as compared with 1.70° (52.70 μm on retina) in normal mice. These values correspond to 0.400 and 0.588 c.p.d. in spatial frequency, respectively, in close agreement with 0.40–0.65 c.p.d. visual acuity of normal mice reported in the literature[38–41]. As a reference, in previous study of RCS rat with PRIMA implant[20], the visual acuity was 34.3, 27.5 and 27.9 μm for pixels of 40 and 20 μm and for natural vision in RCS rat, respectively.

Visual acuity and contrast sensitivity at behavioural level was characterized in optomotor response tests in visual prosthesis studies[6,38,42]. To examine visual acuity and contrast sensitivity in NW-array-implanted blind mice, we conducted an optomotor test (Fig. 3h and Supplementary Video 4). All mice used in visual acuity and contrast sensitivity test were over postnatal day 330, which were earlier tested in the light-source localizing test, moving bar detection test, flashing detection test and orientation discrimination test (details in Methods and Supplementary Table 1). NW arrays were implanted into blind mice for more than 9 months (Supplementary Table 1). A valid head tracking was determined by head angular movements (motor response) in the direction concordant with the stimulus[6,38]. For each spatial frequency and contrast, the clockwise and counterclockwise stimuli were repeated three times, respectively. A qualified optomotor response was defined by at least one valid head tracking trial for both clockwise and counterclockwise stimuli[6]. We did not observe any optomotor response in blind mice with glass implant.

Contrast sensitivity score was defined as the reciprocal of the lowest grating contrast at the fixed spatial frequency[38,43]. In normal mice, the spatial frequency for peak contrast sensitivity was 0.1 cpd, and the contrast sensitivity score was 30 (or 3.3% contrast) (Fig. 3i). The visual

Fig. 4 | Orientation selectivity and in vivo orientation discrimination test. **a**, Schematic of ex vivo patch-clamp recording with contrast reversal gratings at different orientation. Stimuli were projected with 4 Hz flicker frequency and 1 Hz grating alternation (400 nm, 80 μW mm^{-2}). **b**, Responses of representative orientation-selective cells (left) and non-orientation-selective cells (right) in blind retina with NW arrays attached. **c**, Cell response normalized to preferred orientation of orientation-selective cells (n = 4 RGCs from 3 retinas). **d**,**e**, Percentage of orientation selective cells (**d**) and distribution of OSI of RGCs (**e**) in NW-array-attached blind retinas (n = 19 RGCs from 4 retinas). Black lines indicate OSI for each RGC. Dashed green line indicates 0.25 OSI. **f**, Schematics of two-photon calcium imaging in V1 neurons. **g**, Example responses and tuning curves for grating stimuli of orientation selective cells (red) and direction selective cells (green). **h**,**k**, Percentage of orientation-selective cells (**h**) and direction-selective cells (**k**) in stimuli-responsive cells. Normal: n = 4 mice. Blind: n = 8 mice. Blind with NW arrays: n = 10 mice. **i**–**m**, Distribution and cumulative probability distribution of OSI (**i** and **j**) and DSI (**l** and **m**) of stimuli-responsive cells. Normal: n = 1053 cells from 4 mice. Blind: n = 2120 cells from 8 mice. Blind with NW arrays: n = 2,126 cells from 10 mice. **n**, Schematics of the choice-box-based orientation discrimination test. **o**,**p**, Correct rate of orientation discrimination test for each day during the testing trials (**o**) and statistical results (**p**). Normal mice: n = 3 mice. Blind mice with glass implant: n = 3 mice. Blind mice with NW array implant: n = 4 mice. All data are expressed as mean ± s.e.m. Statistical significance was determined using one-way ANOVA with Tukey's multiple comparisons in **h**, **k** and **p**. ***P < 0.001.

https://doi.org/10.1038/s41551-023-01137-8

acuity was defined as the highest spatial frequency of drifting grating with 100% contrast (contrast sensitivity score of 1 in Fig. 3i) that the mouse could track. We plotted the *y* axis in log scale in Fig. 3i to better illustrate data with contrast sensitivity score around 1 (Supplementary Fig. 8). The visual acuity of normal mice was 0.424 ± 0.012 c.p.d. (Fig. 3j), which was consistent with previous reports (0.40–0.43 c.p.d.)[38,41]. For

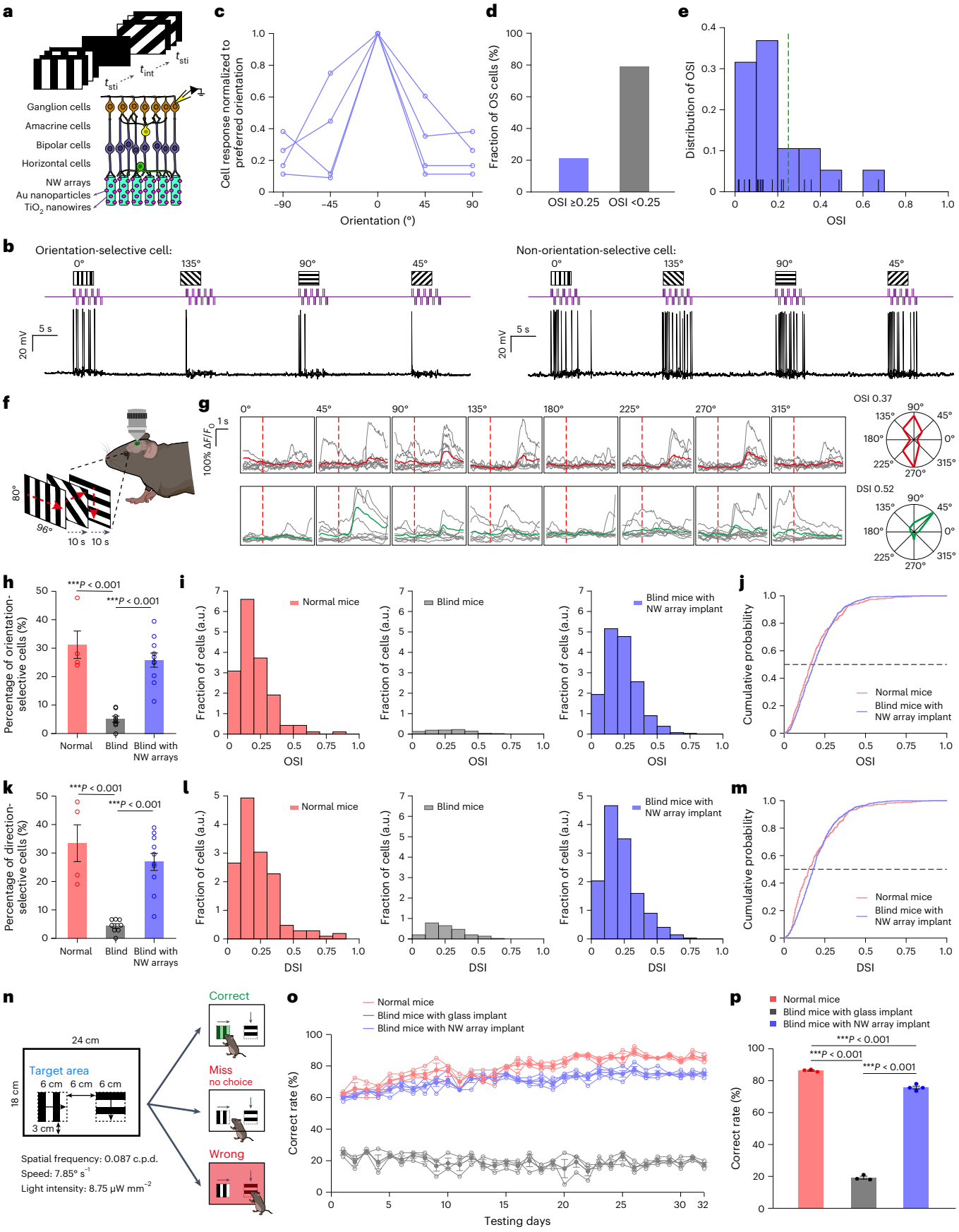

https://doi.org/10.1038/s41551-023-01137-8

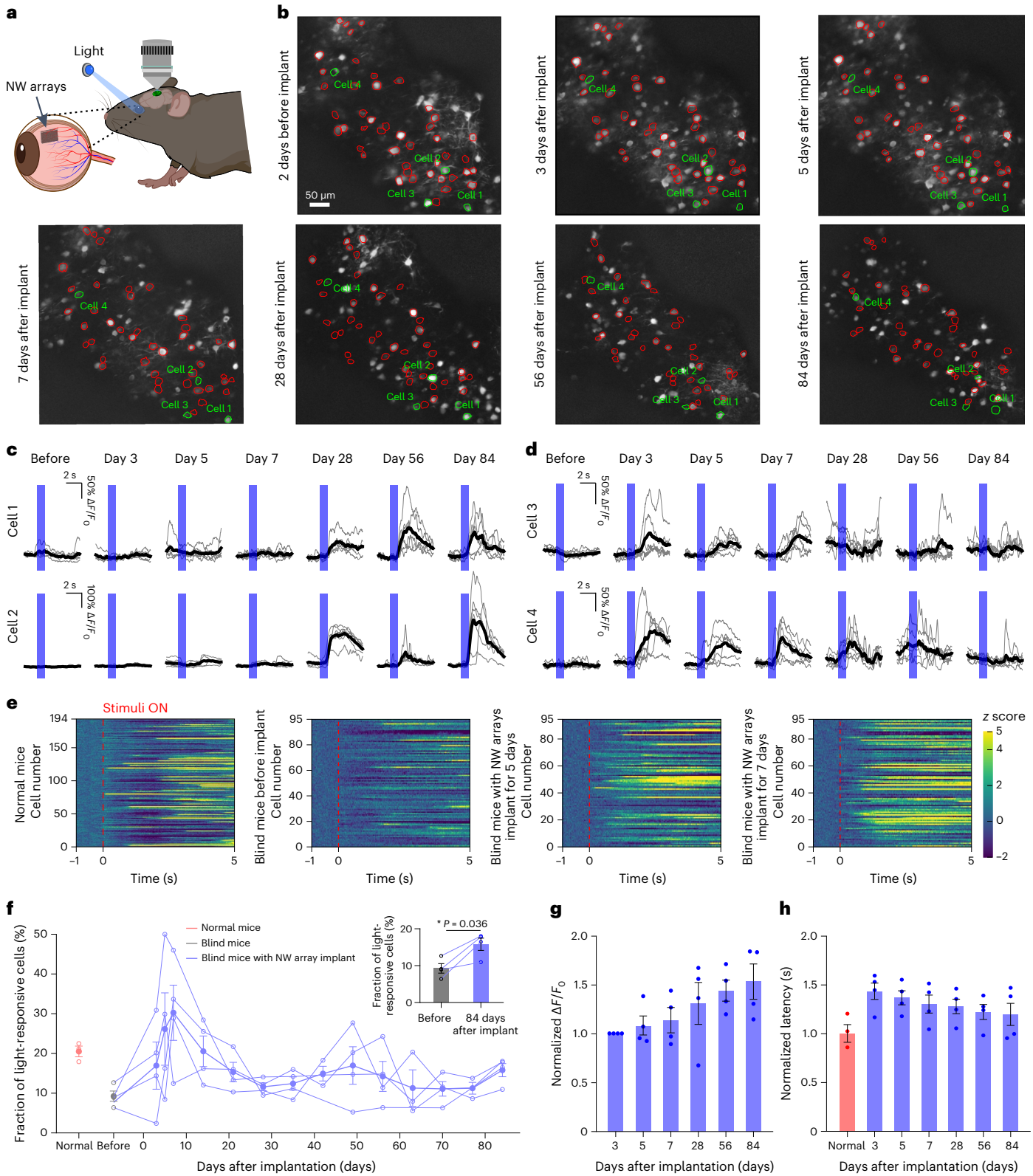

Fig. 5 | Long-term responses to light in V1 neurons of blind mice with the implanted NW arrays. a, Schematics of two-photon calcium imaging in V1 neurons. **b**, Four example neurons (cells 1–4, indicated with green circles) 2 days before implant surgery and 3, 5, 7, 28, 56 and 84 days after NW array implant surgery. Scale bar, 50 μm. **c**,**d**, The fluorescence traces of four example neurons (cells 1–4 in **b**). **e**, Change of GCaMP6s fluorescence (averaged over six trials) in response to blue LED stimulus (wavelength 465/25 nm, intensity 6.75 μW mm^{-2}, duration 1 s) in normal mice ($n = 3$ imaging sites from 3 mice), blind mice ($n = 4$ imaging sites from 3 mice) before implant surgery, 5 and 7 days after NW array implant surgery. Dashed red line indicates the onset of the blue LED stimulus. **f**–**h**, Fraction of light-responsive neurons, normalized $\Delta F/F_0$ and normalized latency of normal mice ($n = 3$ imaging sites from 3 mice), blind mice before and after NW array implant ($n = 4$ imaging sites from 3 mice). All data are expressed as mean ± s.e.m. Statistical significance was determined using two-sided paired *t*-test in **f**. *$P < 0.05$.

NW-array-implanted blind mice, the contrast sensitivity score was 5 (or 20% contrast) and the spatial frequency for peak contrast sensitivity was 0.05 c.p.d. The visual acuity of NW-array-implanted blind mice was 0.313 ± 0.015 c.p.d. (Fig. 3i,j), with significant improvement from blind mice with glass implant.

Previous studies showed that sizes of receptive field for visual cortical neurons are small where visual acuity is high near the foveal region of the cortex in human[44], indicating that the size of receptive field is inversely related to the visual acuity. We first confirmed the retinotopic projection from the NW-array-implanted area in the retina to primary visual cortex (V1). It was previously known that the dorsal nasal retina (where we implanted NW arrays) retinotopically project to medial V1 (refs. 45,46). By injecting DiI in the dorsal nasal retina and CTB 488 in medial V1, we found that DiI and CTB 488 signals overlapped in the dorsal lateral geniculate nucleus (Supplementary Fig. 9a–d). GCaMP6s were largely expressed in V1 neurons (Fig. 3k). Therefore, we conducted two-photon calcium imaging in medial V1 in vivo (Fig. 3k).

Receptive fields of neurons in V1 were mapped using a flashing blue square on a black background and calculated on the basis of calcium signals with Gaussian fitting (Fig. 3l,m). The average size of receptive fields in V1 neurons in normal mice was 233 ± 20 deg^2, which was similar to previous study (246 ± 157 deg^2)[47,48]. In blind mice with NW array implant, the average size of receptive fields in V1 neurons was 403 ± 86 deg^2 (Fig. 3n,o), indicating a similar visual acuity to the normal mice.

Motion perception in blind mice implanted with the NW arrays

Motion perception is one of the key features for visual prosthesis device to restore visual function[35]. Orientation-selective neurons were the neuronal basis of motion perception[49–51]. To test whether blind mice with NW arrays implanted were capable of detecting moving objects, we used alternating gratings with four orientations (60 repeats for each orientation, 0°, 45°, 90° and 135°) to examine the orientation selectivity of RGCs in NW-array-attached blind retina (Fig. 4a). Cells with orientation selectivity index (OSI, Methods) larger than 0.25 had strong responses to the preferred orientation of gratings, while non-orientation selective cells had similar response for all orientations of gratings (Fig. 4b,c). A total of 21.05% of recorded RGCs of blind mice with NW arrays attached exhibited orientation selectivity (OSI ≥0.25, Fig. 4d,e). We also measured responses in V1 neurons to drifting gratings in eight different directions using GCaMP6 recording in vivo (Fig. 4f,g). In blind mice with NW array implant, 28.47% and 26.87% V1 neurons showed OSI ≥0.25 and direction selectivity index (DSI) ≥0.25, which were similar to normal mice and significantly higher than those in blind mice (Fig. 4h–m).

After confirming the NW-array-mediated orientation and direction selectivity in RGC and V1 neurons, we conducted choice-box-based behavioural test for orientation discrimination (Supplementary Video 5). Horizontal and vertical drifting gratings were presented in the target area (Fig. 4n). All mice were over postnatal day 270, and blind mice were implanted with NW arrays or glass for over 7 months, which were earlier tested in the light localization test, moving bar detection test and flashing detection test (details in Methods and Supplementary Table 1). The correct rates for normal mice and blind mice with NW array implant were 86.39% and 75.68%, respectively, significantly higher than that of blind mice with glass implant (19.18%) (Fig. 4o,p). These data suggested that the blind mice with NW arrays implanted was capable of detecting moving objects.

Instead of drifting gratings, moving objects such as light bars were natural stimuli commonly encountered in our daily life[52,53]. In ex vivo experiments, moving light bars elicited action potentials in the RGCs of blind mouse retina attached to NW arrays (Extended Data Fig. 5a–g). Behavioural tests were then conducted in which the reward was associated with a moving light bar (Extended Data Figs. 3e and 5h, and Supplementary Video 6). The performance of normal and NW-array-implanted blind mice was similar for detecting moving light bars, the correct rates being 84.79% and 76.92%, respectively, in detecting moving light bars of 5.25° width and 7.85° s^{-1} (Extended Data Fig. 5i–k).

Light-evoked responses in V1 of blind mice implanted with the NW arrays

Previous study showed that with increasing accuracy in visual stimulus encoding, the responses of neurons in V1 had a shorter latency and a larger amplitude[54]. To investigate whether encoding of NW arrays-mediated responses to visual stimulus improved with time, we conducted long-term two-photon recording from one single neuronal population in V1 at 3, 5, 7, 14, 21, 28, 35, 42, 49, 56, 63, 70, 77 and 84 days after NW array implantation (Fig. 5a,b, Extended Data Fig. 6a and Supplementary Video 7). The total number of recorded neurons in each individual animal did not exhibit significant change over time (Extended Data Fig. 6b). All mice used for two-photon recording were more than 4 months old.

The changes in fluorescence ($\Delta F/F_0$) of 28 representative light-responsive neurons in two mice were shown in Extended Data Fig. 6c–f. Four neurons were persistently visible at 3, 5, 7, 14, 21, 28, 35, 42, 49, 56, 63, 70, 77 and 84 days after implant, among which two neurons started to respond to light 1 month after implantation and remained responsive (Fig. 5c), indicating long-lasting responsiveness[55]. Two other neurons stopped responding to light 1 month after implant (Fig. 5d), indicating the emergence of newly formed responsiveness[55]. The fraction of light-responsive neurons in V1 was 22.41% in normal mice and 15.81% in NW-array-implanted blind 84 days after implantation, significantly larger than that before implant surgery (9.25%, Fig. 5e,f).

In previous studies, after stimulus-associated learning task, the responses of stimulus-responsive cells in V1 had a shorter latency and a larger amplitude, with the accuracy in stimulus encoding increased[54,56]. Interestingly, the fraction of light-responsive neurons peaked around 1 week (26.13% on day 5 and 30.24% on day 7) after NW array implantation (Fig. 5f). The average amplitude of calcium signals gradually increased over time while the latency of light responses decreased over time (Fig. 5g,h), indicating that neurons in V1 exhibited improvement in reliable coding of visual stimulus. These observations were consistent with previous studies, showing that the visual system can retain considerable plasticity beyond critical periods after blindness[57].

Natural scenes are ethologically more relevant than stimuli used in laboratories such as gratings. We also measured the responses in V1 neurons to natural scenes (Extended Data Fig. 7a,b). The fraction of natural-scenes-responsive cells was 72.36% and 56.71% in normal mice and blind mice with NW array implant, respectively (Extended Data Fig. 7c). Responsive selectivity to different stimulus conditions is

Fig. 6 | Ophthalmological characterization of monkeys A and E with the implanted NW arrays. a, Colour fundus photograph of the right eye of monkey A with eight pieces of NW arrays implanted subretinally. The turbid places in the fundus photograph were mainly due to the silicon oil. The yellow arrows indicated the photocoagulation sites. The white arrows indicated the perifovea area for implant surgery. The green arrows indicated photocoagulation sites to seal the opening in the retina. Scale bar, 2 mm. **b**, The retinal structure and the interface between the retina and NW arrays in OCT images of monkey A's right eye. Red-coloured signals indicated the NW arrays. Dark signals indicated the glass substrate for the NW arrays. Scale bar, 1 mm. **c**, Fundus autofluorescence images of monkey A's right eye. Scale bar, 2 mm. **d**, Red-free mode fundus photography of monkey A's right eye. Scale bar, 2 mm. **e**, Colour fundus photograph of the left eye of monkey E with six pieces of NW arrays implanted subretinally. The turbid places in the fundus photograph were mainly due to the silicon oil. Green arrows indicated photocoagulation sites to seal the opening in the retina. Scale bar, 2 mm. **f**, The retinal structure with NW array implant in OCT images of monkey E's left eye. Red-coloured signals indicated the NW arrays. Dark signals indicated the glass substrate for the NW arrays. Scale bar, 1 mm.

https://doi.org/10.1038/s41551-023-01137-8

quantified by lifetime sparseness[58–60]. Neurons in NW-array-implanted blind mice had an average lifetime sparseness of 0.54, similar to that in normal mice (0.61) (Extended Data Fig. 7d).

NW arrays exhibited good biocompatibility and stability

We examined the interface of NW arrays and blind retinas by immunostaining after confirming the light responsiveness of

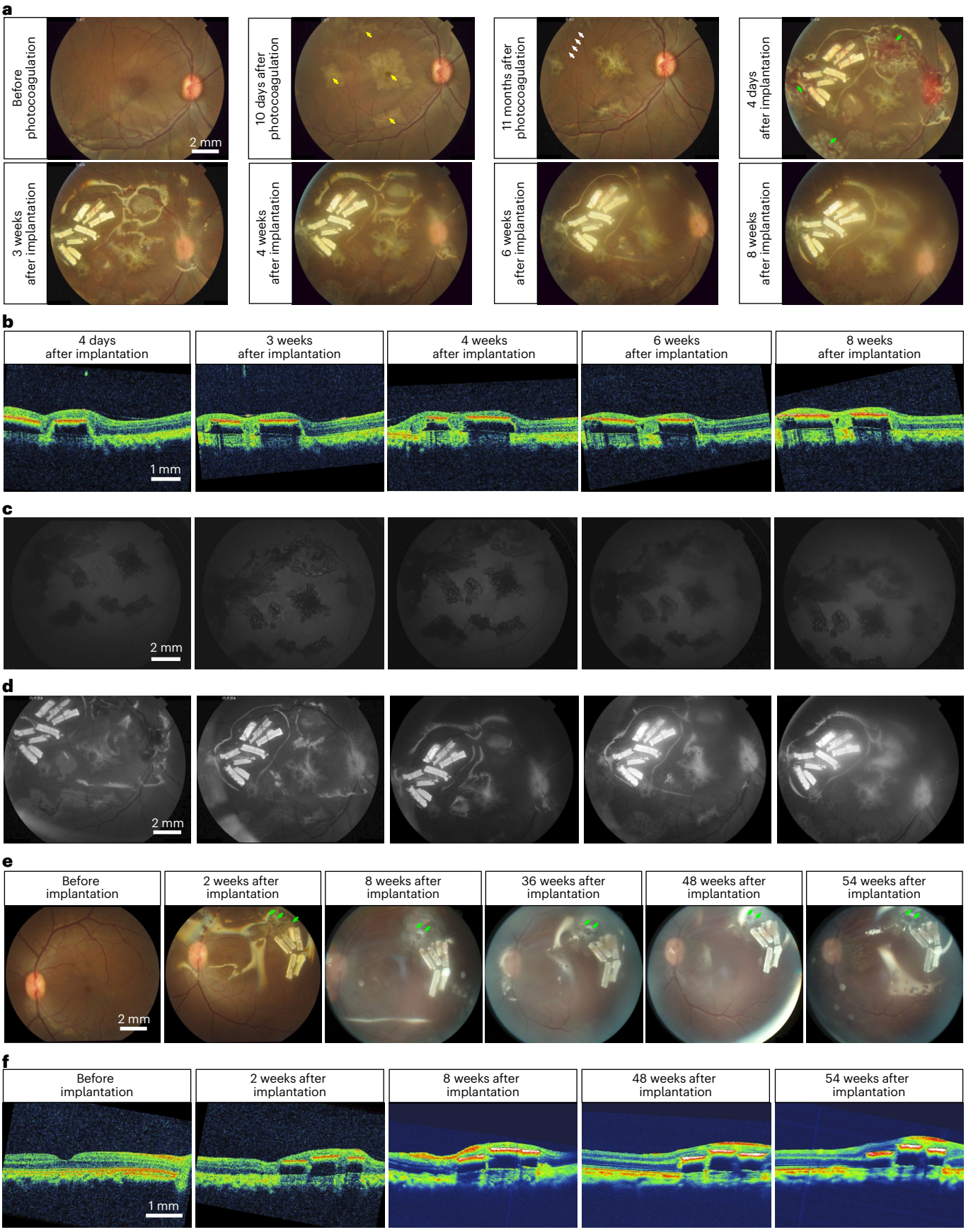

https://doi.org/10.1038/s41551-023-01137-8

NW-array-implanted blind mice by VEP recording, and NW arrays were implanted into blind mice for more than 2 weeks. In three-view diagram (Extended Data Fig. 8a,b), the NW arrays were marked by the white contour in the x–y plane or the bulges in the x–z and y–z planes. Three-dimensional reconstructed models of retina at the borders of the implants showed that the retina was in good consistency when elevated by the implant (Extended Data Fig. 8c). Cell numbers of bipolar cells and RGCs from the interface were in good accordance with those from the outskirts 2 weeks, 4 weeks and 6 months post implantation (Extended Data Fig. 8d,e).

In blind retina, rod bipolar cells (RBPs) had one or two dwarfed dendrites with no bifurcation or dendritic spine (Extended Data Fig. 8f), consistent with previous study[61]. Interestingly, the (contralateral) NW-array implanted retina exhibited a considerable number of RBPs at the material–tissue interface with strengthened dendrites as well as multiplied dendritic bifurcations. RBPs with similar dendritic features could also be found in the material–tissue interface 2 weeks post implantation (Extended Data Fig. 8g,h). These results suggest that the observed structural deviations of RBP dendrites from the canonical murine RP models are probably due to the NW array integration in the material–tissue interface with time.

Eyeballs of mice are much smaller than those of primates. More importantly, unlike primates, rodents have no fovea. We implanted NW arrays in two eyes of two monkeys. We first conducted photocoagulation on the fovea and perifovea areas in the right eye of monkey A to induce focal photoreceptor degeneration (indicated by the yellow arrow in Fig. 6a). Due to the coronavirus disease 2019 (COVID-19) pandemic, we were not able to conduct the implant surgery until 11 months after photocoagulation, when the presence of scar tissue in the photocoagulated area was not optimal for implant surgery. At 11 months after photocoagulation, the fixation ability of monkey A had recovered compared with that at 2 weeks after photocoagulation, and was close to the level before photocoagulation (Extended Data Fig. 9a). Instead of conducting surgery on the photocoagulated area, we identified an intact perifovea area to conduct implant surgery (indicated by the white arrow in Fig. 6a).

Retinal prosthesis devices were implanted following a 23-gauge vitrectomy[23]. To minimize the surgical trauma on the sclera and retina, NW arrays were cut into 0.40 mm × 1.80 mm pieces to be fit into the 23-gauge trocars for vitrectomy. We delivered NW arrays through 23-gauge trocars using forceps, and eight pieces of NW arrays were subretinally inserted. Finally, we injected perfluoro-decalin liquid over the NW arrays to stabilize the implant, and injected silicone oil into the vitreous cavity to support retinal re-attachment. Photocoagulations were conducted to seal the opening in the retina from retinotomy (indicated by green arrows in Fig. 6a).

Colour fundus photography at 4 days and 3, 4, 6 and 8 weeks after implant surgery showed that NW arrays stayed in place (Fig. 6a). Optical coherence tomography (OCT) showed that the retina and NW arrays were in close contact throughout 8 weeks after implantation (Fig. 6b). There were no significant changes in RPE cells in autofluorescence images (Fig. 6c). Red-free fundus photography indicated no vascular abnormality in the retina and surrounding tissue after NW array implantation (Fig. 6d).

Unlike monkey A, the second monkey (monkey E) was not photocoagulated before NW array implant. Six pieces of NW arrays were implanted subretinally into the left eye of monkey E. Colour fundus photography 2, 8, 36, 48 and 54 weeks after implantation showed that NW arrays stayed in place (Fig. 6e). OCT results showed that the retina and NW arrays were in close contact throughout 54 weeks after implantation (Fig. 6f). Due to lab-access restrictions caused by the COVID-19 pandemic, we were not able to collect data of colour fundus photography and OCT using the same instrument. Together with results from monkey A, these data suggested that NW arrays were stable in subretinal space and exhibited good biocompatibility in monkeys.

Light-induced saccades in monkeys implanted with the NW arrays

We conducted monocular VGS behavioural test to investigate the NW-array-mediated light-responsiveness in monkeys (Fig. 7a–c). The non-surgical eye was covered by eyeshade. Monkeys A and E were trained to fixate at the central fixation point (beam angle: 0.5°, 125 µm on the retina) at the beginning of the task. A target point (beam angle: 0.5°, 125 µm on the retina) appeared 1 s later. If the monkeys shifted their gaze from the central fixation into the target area (defined as a 15° circular region surrounding the target points, Extended Data Fig. 9b–d) within 1 s, the trial was defined as a correct trial.

Monkey with glass implant would be an ideal control from one animal to another. However, due to ethical and logistics reasons against additional monkeys for surgical implantation with inert material(s), we used red LED (642/18 nm) to map out the visual field as a within subject, trial control, since NW arrays generated photocurrent upon UV, blue and green, but not red stimulation. In addition, a previous study confirmed the photoreceptor degeneration at the implant region by showing that photovoltaic subretinal prosthesis in monkeys blocked nutrient flow to the retinal area adjacent to the implant, which caused consecutive separation from the underlying retinal pigment epithelium/choroid[23]. In monkey A, the hit rate (the number of correct trials divided by all trials) for red light stimuli in the implanted region decreased from 86.7% (before implant) to 56.7% (5–7 weeks after implantation) and 35.7% (10–12 weeks after implantation) (Extended Data Fig. 9e–h,l and Supplementary Video 8). Fourteen to 15 weeks after implantation, the hit rate for red light stimuli in the implanted region was 12%, suggesting the degeneration of photoreceptors. Similar to monkey A, the hit rate of monkey E for red light stimuli before implantation and 18–20 weeks after implantation were 97.6% and 22.03%, respectively (Fig. 7g–i). At 18–20 weeks after implantation,

Fig. 7 | VGS behaviour for monkeys A and E with the implanted NW arrays. **a**,**b**, Schematics of VGS behavioural task for monkeys with NW array implant. **c**, NW arrays in the fundus photographs of monkey A (polar angle 190–270°, eccentricity 19° and 21°) and monkey E (polar angle 310–330°, eccentricity 17°) that were overlaid onto the visual field. Scale bar, 2 mm. **d**, Illustration of mean hit rates in VGS task of monkey A with red and UV LED stimuli (0.5°, polar angle 190–270°, eccentricity 19° and 21°) before implantation and 14–15 weeks after implantation. **e**, Example saccadic trace of monkey A in response to red or UV stimuli in the target points, corresponding to **d**. **f**, Hit rates of monkey A in VGS task. Left: hit rates of normal regions and NW-array-implanted regions with different light intensities (0.60–10.00 µW mm^{-2}). Red LED stimuli in normal region, n = 69 sessions. UV LED stimuli in implanted region, n = 44 sessions. Blue LED stimuli in implanted region, n = 37 sessions in implanted region. Red LED stimuli in implanted region, n = 11 sessions in implanted region. Right: mean hit rate with stimuli in implanted regions before implantation (red LED stimuli, light intensity: 7.58 µW mm^{-2}, n = 20 sessions) and 14–15 weeks after implantation (red, blue and UV LED stimuli, light intensity 10.00 µW mm^{-2}, n = 5 sessions for each group). **g**, Illustration of mean hit rates in VGS task of monkey E with red and UV LED stimuli (0.5°, polar angle 270–330°, eccentricity 17°) before implantation and 18–20 weeks after implantation. **h**, Example saccadic traces of monkey E in response to red or UV stimuli in the target points, corresponding to **g**. **i**, Hit rates of monkey E in VGS task. Left: hit rates of normal regions and NW-array-implanted regions with different light intensities (1.65–8.52 µW mm^{-2}). Red LED stimuli in normal region, n = 11 sessions. UV LED stimuli in implanted region, n = 64 sessions. Red stimuli in implanted region, n = 43 sessions. Right: mean hit rate with stimulus in implanted regions before implantation (red LED stimuli, light intensity 8.52 µW mm^{-2}, n = 21 sessions) and 18–20 weeks after implantation (red and UV LED stimuli, light intensity 8.52 µW mm^{-2}, n = 15 sessions for red LED stimuli, n = 23 sessions for UV LED stimuli). All data are expressed as mean ± s.e.m. Statistical significance was determined using one-way ANOVA with Tukey's multiple comparisons in **f** and **i**. ***P < 0.001.

https://doi.org/10.1038/s41551-023-01137-8

monkey E had low mean hit rate (below 25%) and could not accurately saccade to the red-light stimuli in implant regions (polar angle 310–330°), while the mean hit rate of normal regions (polar angle 270–290°) was still above 80% (Fig. 7g,h). In addition, with red light stimuli (642/18 nm, 10 μW mm^{-2}) in normal regions, the hit rate of monkey A was more than 80% (Extended Data Fig. 9d and Supplementary Table 2), suggesting that monkeys were capable of performing VGS task after implantation surgery.

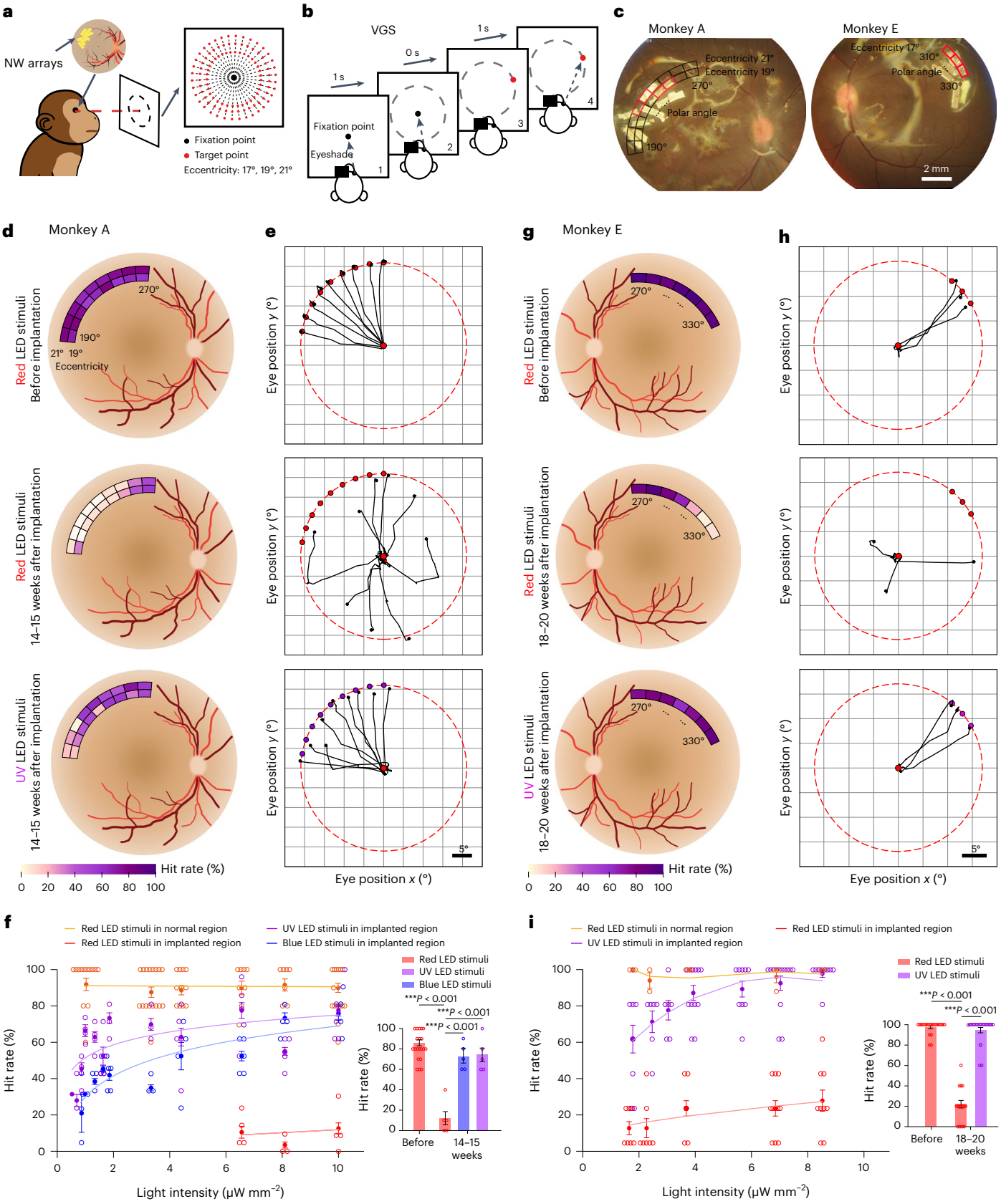

To examine the NW-array-mediated light responses, we used blue (465/25 nm) and UV LED (360/15 nm) light to stimulate the NW-array-implanted area (Fig. 7d,e, Extended Data Fig. 9i–k and Supplementary Video 9). Note that the intensity of UV light we used was lower than that reported for solar light in the late summer afternoon in previous studies and also much lower than the known damaging thresholds of UV (30 μW mm^{-2}) for the corneal endothelium, lens and retina[62]. For monkey A, when using red light stimuli, 95.58% of the endpoints were outside the target area, whereas when stimulating with UV or blue light, 80.28% of the endpoints located within the target area (Extended Data Fig. 9h,i). The mean hit rates elicited by blue and UV light were 72.5% and 74%, respectively, at 10.00 μW mm^{-2} (Fig. 7f), which was significantly larger than that in red light (12%). The latency of saccade was defined as the time from the target point onset to the saccade onset. For monkey A, the mean latency for normal saccade under UV LED stimuli was 357.26 ms (Extended Data Fig. 10a). After NW array implantation, the saccade latency was 349.67 ms.

Monkey E also exhibited responsiveness to UV but not red light (Fig. 7g,h). The mean hit rate of UV light was 93.7% at 8.52 μW mm^{-2}, which fell below 60% when the light intensity was below 1.78 μW mm^{-2} (Fig. 7i). For monkey E, the mean saccade latency was 378.74 ms before implantation and 369.79 ms after implantation (Extended Data Fig. 10a). Due to lab-access restrictions caused by the COVID-19 pandemic, we were not unable to collect data for blue light in monkey E. These results indicated that stimulating NW arrays induced saccade behaviour in a non-human primate, were able to rescue light responses in photoreceptor-degenerated area.

Discussion

TiO_2 is one of the most reported inorganic semiconductors, of which the synthesis method and the working principle have been well established. It possesses the advantages of non-toxicity, high stability and low cost. In addition, it can enable adsorption for wide-range wavelength light by tuning the bandgap via Au decoration and oxygen vacancy introduction. In this study, we demonstrated an NW-array-based retinal prosthetic device with high sensitivity. After improving the fabrication process in the NW arrays from our previous study[30], a correct rate of 83.3% is demonstrated for a light intensity as low as 2.93 μW mm^{-2} in mice behavioural experiment. Likewise, monkeys can achieve a hit rate of 72.5% at 10.00 μW mm^{-2}. The intensity of UV light stimuli in our study was lower than that for solar light in the late summer afternoon and much lower than the known damage thresholds of UV (30 μW mm^{-2}) for the corneal endothelium, lens and retina[62]. Although a recent study reported activation of retinal and V1 cells in the order of μW mm^{-2} using Channelrhodopsin variant, no behavioural evidence with low irradiance was presented[63]. Hence, to the best of our knowledge, our NW array is among the state-of-the-art retinal prosthetics with very high light sensitivity. Augmentation strategies such as video goggles with light amplification function[8,23] may further help enhance visual responses in dark environment.

One important feature for image-forming vision is spatial resolution. In the clinical trials of subretinal implant Alpha-IMS, even though a grating acuity of 3 c.p.d. was reported in one patient, the majority of patients had low acuity and were not able to read[64]. For RCS rat with PRIMA implant[19,20], the prosthetic vision measured by VEP recording was improved with decreasing pixels of implants, reaching the limit of natural visual resolution in rats with 20 μm pixels. In our study, the NW-array-implanted blind mice were capable of detecting moving light bars with a spatial resolution of 0.313 c.p.d. A high-density NW arrays[26] could potentially pave the way for restored vision with better spatial resolution.

Interestingly, the fraction of natural scenes responsive cells in blind mice was not zero (16.69%). However, we have already confirmed that all photoreceptors including rods and cones degenerated as early as P50 in *rd1*/*cDTA* mice (Supplementary Fig. 3). Previous study also reported non-zero light responses in blind mice[27]. There are evidences that level of spontaneous activity in RGCs is higher in blind mice than that in normal mice[65–67]. In addition, the average spontaneous firing rate in V1 neurons for degenerated rats was significantly higher than that for normal rats[68]. This evidence suggests that the responses in V1 neurons in blind mice were probably from spontaneous activities.

Previous study showed that sustained RGCs detect the form, size and shape, while transient RGCs detect the motion or location of the input[69]. In both our previous study[30] and the current study, we reported both sustained-ON and transient-ON responses in the RGCs recordings. As for temporal resolution, NW-array-implanted blind mice were capable of discriminating 1–5 Hz flashing stimuli. RGCs in blind retina with NW arrays attached could respond to 0.5–20 Hz flicker frequency, and the threshold of temporal frequency was 3.92 Hz in NW-array-attached blind retina with flashing stimuli (400 nm, 80 μW mm^{-2}), which was 4.01 Hz in normal retina. These results indicate that NW arrays improved primary visual functions such as temporal and spatial resolution in blind mice.

Despite the fact that no chronic inflammation or cell loss was detected in blind mouse retinas with NW array implant, saccade experiments in monkeys suggested that in-situ photoreceptors degenerate at the implant site, which is also observed in other subretinal prosthesis in primates[23]. Since the NW arrays did not respond to red light stimuli, responses to red stimuli were used as within subject, trial control in behavioural test of monkeys with NW arrays implanted. However, using red stimulation as control could not rule out the possibility that red photoreceptors went through a faster degeneration process than blue photoreceptors post NW array implant, in which case some response to the blue stimulation might be mediated by remaining blue photoreceptors. Therefore, monkey with glass implant would be an ideal control. Unfortunately, due to ethical reasons, proposal for glass implant surgery in monkeys was not approved. For clinical applications, NW arrays and other subretinal implants are suitable for patients with complete loss of photoreceptors, including late-stage RP and geographic atrophy[17]. Moreover, for patients with partial vision loss, such as patients with AMD with residual peripheral vision, visible light (blue or green light) may be a better option. Augmented reality glasses such those used in PRIMA[18] can be also used to convert visual stimuli into UV light and project them directly to the implant NW arrays. In addition, subretinal implants can be applied in the retinal region with impaired vision, and gene therapy can be used in other retinal regions with reduced vision to prevent further vision loss. In this case, subretinal implants are in principle compatible with gene therapy and other restoration methods, in which gene therapy delays the degeneration of photoreceptors at early stage and prevents further vision loss, whereas subretinal implants would be helpful to restore vision in the region with severe photoreceptor degeneration.

For the VGS task in monkeys, the target point was presented for 1 s, which was longer than the mean saccade latency (340–380 ms, Extended Data Fig. 10a). We then presented the illumination for 250 ms instead, in which 96.67% trials had a saccade latency of >250 ms (Extended Data Fig. 10b), indicating no activation on the path to the target point. There was no significant difference in both hit rate and target distance (distance between the saccadic endpoint and the target point in correct trials) of the VGS task between 1,000 ms and 250 ms illuminations in NW-array-implanted region (Extended Data Fig. 10c,d). These results suggest that 250 ms illumination did not result in the improvements in either the performance or the precision of VGS task; hence, the activation on the path to the target point does not contribute to the VGS task in our experiments.

One intriguing observation from our data was the transiently enhanced responses during the first week post implant together with continuously improving response reliability in the visual cortex of blind mice. The performance level of NW-array-implanted mice in 4-week group at localizing the LED was better than 1-week group. In addition,

a previous study of a polyimide-based subretinal implant in P23H rats showed a monotonic increase in the electrode impedance within the first three weeks, followed by stabilized impedance[70]. Increasing impedance corresponded to decreasing stimulation threshold[70], indicating the improvement in the electrode–retinal–tissue interface within the first three weeks. And another study of subretinal implant also reported that the impedances increased continuously within 20 days after subretinal implantation and stabilized afterwards[71]. Therefore, an improved retinal–tissue/NW-array interface within the first few weeks after implant surgery may contribute to the improved visual performance in 4-week group.

Together, these results indicated that even in adults who are well beyond the age of the critical period, the sensory cortex retains certain levels of plasticity, which potentially leads to the functional rewiring of the visual cortex and improved visual function.

Methods

Synthesis of TiO_{2-x} NW arrays and $AuTiO_{2-x}$ NW arrays

In a typical synthesis, 0.5 ml tetrabutyl titanate was added into the mixture solution of 15 ml de-ionized water and 13 ml hydrochloric acid (HCl) to form transparent solution by stirring. Then, fluorine-doped tin oxide (FTO) glass substrate was treated by piranha solution (H_2SO_4/H_2O_2 with volume ratio of 7:3) to obtain the hydrophilic surface. Afterwards, both of solution and FTO were transferred into a 50-ml Teflon-lined stainless-steel autoclave, and heated to 150 °C for 12 h to grow TiO_2 NW arrays. Next, the TiO_2 NW array-coated FTO glass was annealed at 550 °C for 3 h with a heating rate of 5 °C min^{-1} in the air to increase the crystallinity. After that, it was further annealed under 350 °C in 5% H_2/Ar atmosphere for 12–36 h, with a flowing rate of 150–200 standard cubic centimetres per minute to obtain the TiO_{2-x} NW arrays with oxygen vacancies. Then, the FTO substrate with TiO_{2-x} NW arrays was immersed into the 0.01–0.1 M $HAuCl_4$ aqueous solution and adjusted the solution pH value around 4.5 by adding 0.2 M NaOH aqueous solution. After incubating for 2 h, the FTO substrate was taken out, dried and annealed under 300 °C for 2 h with a heating rate of 5 °C per min in the Ar atmosphere. Finally, the FTO substrate was etched at 85 °C in a mixed solution of H_2SO_4/HF (40 wt%) with the volume ratio of 13:2.

Photocurrent measurement

The photocurrent was measured using a setup consisting of a Zeiss upright DIC microscope (Examiner A1, Zeiss) and a three-electrode system. The $AuTiO_{2-x}$ NW array photoanode, a coiled Pt wire and an Ag/AgCl were used as working, counter and reference electrodes, respectively. Phosphate-buffered saline (pH 7.4) was used as the electrolytes. A glass pipette (resistance within 4.8–5.2 MΩ) filled with phosphate-buffered saline was attached to the NW arrays, and its photocurrent was recorded. Near UV, blue and green light was generated from the mercury lamp (X-Cite 120, Lumen Dynamics), filtered by fluorescence cubes (UV: 375/28 nm; blue: 470/20 nm; green: 546/12 nm, Zeiss) and provided through the ×40 water-immersion objective.

Animals and genotyping

Mice were raised and bred at 23 ± 2 °C room temperature, 60–65% relative humidity and a 12 h light/12 h dark cycle. The wild-type (C57BL/6J) mice were purchased from the Slac Laboratory Animal Co. To differentiate between *cDTA*-positive and rd1 homozygote mice, we employed two sets of primers and a restriction enzyme (ThermoFisher, HpyF3I (DdeI)), which recognizes C^TNAG sites. To distinguish between $rd1^{-/-}$ and $rd1^{+/-}$ mice, we used the primers 5′-CATCCCACCTGAGCTCACAGAAAG-3′ and 5′-GCCTACAACAGAGGAGCTTCTAGC-3′. After digestion, homozygote mice exhibited two mutant bands at 126 bp and 155 bp, while heterozygous mice displayed two mutant bands and a wild-type band, with mutant bands at 126 bp and 301 bp. To differentiate between *cDTA* knockout and wild-type mice, we used the primers 5′-CAAGGAAATTATGACGATGATTGG-3′ and 5′-GGCTTGAGCCATATACTCATACATCGC-3′, resulting in a mutant band at approximately 450 bp.

With the exception of the behavioural experiments, which exclusively used male mice, the other experiments were conducted using mice of unspecified gender. Details about age were reported in the corresponding section of Results and Supplementary Table 1. The *n* number for each experiment can be found in the corresponding figure legends. The experimental procedures for mice were approved by the Animal Ethics Committee of School of Basic Medical Sciences at Fudan University.

Two male macaque monkeys (*Macaca mulatta*) used in this study were bred in East China Normal University, Shanghai (monkey A: 12 years old and 8 kg; monkey E: 12 years old and 13 kg). The experimental procedures for rhesus monkeys were approved by the Institutional Animal Care and Use Committee at East China Normal University (protocol number Mo20200101).

Patch-clamp recording of RGCs in mouse retina

Mice were anaesthetized with isoflurane (1–2% at 0.5–1.0 l min^{-1}). Enucleation was conducted on one eye, which was quickly placed in oxygenated Ringer's solution (in mM, NaCl 124, KCl 2.5, $CaCl_2$ 2, $MgCl_2$ 2, NaH_2PO_4 1.25, $NaHCO_3$ 26 and glucose 22, pH 7.35; oxygenated with 95% O_2 and 5% CO_2). For patch-clamp recording of retinal ganglion cells (Fig. 1a), the bottom layer was the NW arrays, with the NWs facing upwards. Above the NW arrays was a piece of filter paper (Merck Millipore) with a hole in the centre (indicated as dashed green lines in Fig. 1a). The retina was positioned onto the filter paper with the outer retina facing downwards, in direct contact with the NW arrays through the hole in the filter paper. A metal grid was placed on top of the retina, ensuring that the retina was in close contact with the underlying NW arrays. In recording of blind mice with glass attached, the NW arrays was replaced with glass of the same size. A glass pipette (resistance 5–10 MΩ) was pulled by P-97 micropipette puller (Sutter Instruments) and filled with internal solution (in mM, potassium gluconate 105, KCl 5, $CaCl_2$ 0.5, $MgCl_2$ 2, egtazic acid 5, HEPES 10, Mg-ATP 4, GTP-Na 0.5 and sodium phosphocreatine 7, pH 7.4). Data were acquired by MultiClamp 700B patch-clamp amplifier (Molecular Devices) and digitizer Digidata 1440 (Molecular Devices) under DIC microscope (Zeiss)[72]. Data were pre-processed by CED spike2 v7.16 (Cambridge Electronic Design) and customized Python code.

Visual stimuli were provided by mercury lamp (X-Cite 120PC Q, LUMEN DYNAMICS) and DMD (wavelength 400 nm). To investigate the response of RGCs to the light with different wavelengths, UV, blue or green light was presented by mercury lamp. DMD was used to present moving and static bars, flashing light and alternating grating visual stimuli. Moving light bars (width: 20, 40, 60, 80, 100, 120, 140, 160 and 180 μm, speed: 200 μm s^{-1}) were presented in a 300 μm width screen ten times in 30 s. Static light bar remained on for 30 s. Different temporal frequencies (0.5–20 Hz) of flashing stimuli were used to examine the temporal resolution of the RGCs, and different widths (3–200 μm) of the alternating gratings with reversing the contrast at 1 Hz were used to examine the spatial resolution of the RGCs.

Clampfit (Axon) was used to analyse the action potentials of RGCs and Prism v9.5 (GraphPad) was used to analyse firing rates and fraction of responses. Firing rate was the number of action potentials per seconds during visual stimulation. We provided ten stimulations (trials) and repeated three times for each RGC. A responsive trial was defined when action potentials were elicited during the stimulation. The fraction of response was calculated as the mean number of responsive trials divided by ten trials.

NW array implant surgery in mice

The *rd1*/*cDTA* mice (blind mice) aged 8–10 weeks were anesthetized with isoflurane (1–2% at 0.5–1.0 l min^{-1}). The eyeball was fixed in a suitable position for implantation by suturing the upper and lower eyelids.

A small incision was made on the dorsal sclera. Then 1–2 µl of 0.9% sodium chloride solution was injected subretinally with NanoJect II (Drummond Scientific Company) to induce retinal detachment. The incision was further expanded to make enough space for the NW array implant. The area of NW arrays was 0.5–1 mm^2. The NW arrays were sterilized before implantation, and then the NW arrays were held by tweezer and inserted subretinally through the incision. After the implantation, the suture was removed, and the eyeball was washed with 0.9% saline solution and applied with erythromycin eye ointment.

Choice-box-based behavioural test

The choice box (240 mm × 240 mm × 180 mm) was customized using acrylic sheets, containing a water delivery system (Kamoer, composed of water pipe, water port and water pump) and an audio signal system (a buzzer positioned in the middle of the choice-box lid). Visual stimuli were placed at two positions (12 cm apart). Light intensity of all visual stimuli in this behavioural task was measured at 6 cm away from the light source. Visual stimuli, water delivery system and the audio signal system were all controlled by Arduino.

Choice-box-based behavioural test was divided into training trials and testing trials[73]. Mice were water restricted for 3 days before the training trials. The mice could explore the choice box freely for 5–10 min before the trials started. During the training trials, stimulation duration was the maximal duration of visual stimulation, if the mice did not touch the screen, the visual stimulation would last 20 s in training trials and 10 s in testing trials. If the mice touch the screen during the visual stimulation, the visual stimulation would be closed and reward would be provided or not. Interval was defined as the time between the mouse touching the screen and the start of the next stimulus (Fig. 1g). The trial started by cueing with audio signal (tone 1). After 3 s, the visual stimulus appeared randomly at one of the two visual stimulation locations. The mice were trained to touch the target area (defined by a circle centred at the LED with a beam angle of 6 cm in light localization test) by their paws or noses. If the mice picked the right visual stimuli within the stimulation duration, another audio signal (tone 2) by the buzzer will be given and the mice were able to obtain water reward at the water port (defined as a correct trial). If the mice failed to touch the screen within stimulation duration, the trial was defined as a miss trial, the audio cue (tone 2) and water reward would not be provided. If the mice touched area outside the right visual stimuli region on the screen within stimulation duration, the trial was defined as a wrong trial, the audio cue (tone 2) and water reward would also not be provided. The next trial would start when the mice stayed away from the visual stimulation region.

When the miss rate of normal mice became less than 50% for more than 3 days in training trials, the behaviour paradigm of all mice was switched to testing trials. No mice were excluded from the behavioural task in this study. The protocol used in testing trials was similar to that in the training trials, except that the stimulation duration was reduced to 10 s, and the interval between each trial was 5 s.

One batch of blind mice were used in choice-box-based behavioural test and the optomotor test. After NW arrays or glass implanted, this batch of blind mice was trained to conduct light localization test, moving bar detection test, flashing detection test, orientation discrimination test and optomotor test in sequence.

In the light localization test, LED lights with different wavelengths and intensities were used. LED visual stimuli appeared randomly at one of the two visual stimulation locations. In the testing trials, UV LED light (375/15 nm, 6.24 µW mm^{-2}), blue LED light (465/25 nm, light intensities: 6.75, 3.31, 2.93, 1.53 and 0.64 µW mm^{-2}), and green LED light (535/28 nm, light intensities: 7.83, 4.20, 2.04 and 1.15 µW mm^{-2}) were used. In Supplementary Fig. 6b,c, LED light was provided at 20 Hz flicker frequency (duration 25 ms).

In the experiment of discriminating moving and static light bar, the visual stimulus was presented by the projector (CB-S41, EPSON). The two visual stimulation regions in one single screen maintained equal light intensity during the test. A moving light bar stimulus was presented randomly at one of the two visual stimulation locations, and a static light bar stimulus was presented at the other position simultaneously. Mice would be rewarded with water if they touched the target area associated with the moving light bar. In the testing trials, static or moving light bar stimuli with different widths (widths: 2.63°, 3.94°, 5.25°, 6.57° and 7.88°, velocity: 7.85° s^{-1}) and velocities (velocities: 5.23° s^{-1}, 6.54° s^{-1}, 7.85° s^{-1}, 9.18° s^{-1} and 10.47° s^{-1}, width: 5.25°) were used.

In the experiment of discriminating flash stimulus and constantly bright light stimulus, the visual stimulus was also presented by the projector. The two visual stimulation regions in one single screen maintained equal light intensity during the test. A flashing stimulus (6 cm × 6 cm square) was presented at one of the two visual stimulation regions randomly, and the constantly bright light stimulus was presented at the other position simultaneously. Mice would be rewarded with water if they touched the target area associated with the flashing stimulus. In the testing trials, temporal frequencies of 1, 1.25, 2, 3.33 and 5 Hz were used for the flash stimulus.

In the experiment of discriminating different orientation drifting gratings, the visual stimulus was also presented by the projector. The two visual stimulation regions in one single screen maintained equal light intensity during the test. The horizontal drifting gratings (spatial frequency 0.087 c.p.d., speed 7.85° s^{-1}, light intensity 15.07 µW mm^{-2}) were presented at one of the two visual stimulation regions randomly, and the vertical drifting gratings were presented at the other position simultaneously. Mice were trained to touch the target area associated with horizontal drifting grating to get water reward.

Visual acuity and contrast sensitivity measurement

To measure the visual acuity and contrast sensitivity, we designed a system with four liquid-crystal display monitors arranged in a quadrangle, and a camera was installed over the system for video recording. Visual stimulus (drifting black and white gratings, 12° s^{-1}) was generated by the Psychopy toolbox[74]. The direction of drifting gratings was switched between clockwise and counterclockwise. Each direction lasted for 10 s and was repeated three times. One day before testing, each mouse was habituated to staying on the pedestal (height 12 cm, radius 4 cm) for 5 min. On the testing day, each mouse was placed on the pedestal and allowed to move freely. The test was paused and resumed if the mouse slipped or jumped off the pedestal. Grey background was presented on the screen at the beginning of each session. When the mouse stopped moving, the grey background was replaced with drifting grating with the mean luminance at 100% contrast and the spatial frequency at 0.1 cycles per degree. Clockwise and counterclockwise drifting grating were presented three times, respectively. A valid head tracking trial was defined by head angular movements (motor response) in the direction concordant with the stimulus[6,38]. An optomotor response was qualified when there were at least one valid head tracking trial for both clockwise and counterclockwise stimuli[6]. After optomotor response was observed, the spatial frequency was increased by 0.05 cycles per degree in the next successive trials until the mouse did not have optomotor response. The highest spatial frequency of drifting grating that the mouse had optomotor response at the grating contrast of 100% was identified as the visual acuity.

In contrast sensitivity test, grey background was also presented on the screen at the beginning of each session and replaced with drifting grating when the mouse stopped moving. The contrast sensitivity was examined at eight fixed spatial frequencies (0.031, 0.045, 0.064, 0.092, 0.130, 0.192, 0.272 and 0.350 cycles per degree). The contrast sensitivity test started with gratings at 0.031 cycles per degree and 100% contrast. After optomotor response was observed, the contrast decreased in the next successive trials until the mouse did not have optomotor response. The lowest contrast of drifting grating that the

mouse had optomotor response at the grating with 0.031 cycles per degree was identified as the contrast threshold. Then contrast threshold of another spatial frequency was examined. The contrast sensitivity at each spatial frequency was computed as 1/contrast threshold. The contrast sensitivity of blind mice with glass implant that had no optomotor response was set to 0.

VEP recording and analysis

Mice were anaesthetized with isoflurane (1–1.5% at 1–1.5 l min^{-1}) and placed on a warming pad (37 °C) to maintain body temperature during the surgery. Eye ointment was applied with a cotton swab to keep the mouse's cornea moist. Then we clipped off the head skin and clear the connective tissue to achieve good exposure of the skull. A 2.5-mm-diameter craniotomy over primary visual cortex was performed on the right hemisphere, starting at the 2.3 mm lateral and 3.3 mm posterior of bregma point. The skull was thinned by cranial drill and soaked carefully in sterile saline solution. The silicon electrode (A4 × 8–5 mm, Neuronexus) was implanted into the primary visual cortex at a depth of 0.2–0.4 mm by micromanipulator (Scientifica). All blind mice used in this experiment had been implanted with NW arrays for more than 2 weeks.

To measure the visual acuity, alternating gratings of various spatial frequencies (grating stripe width 1.4–17°, flicker frequency 4 Hz (an integer closest to 3.92 Hz temporal frequency), grating contrast reversal 1 Hz, corresponding to a contrast reversal every 500 ms) were generated by Psychopy toolbox[74] and presented by DMD (400 nm, light intensity 80 μW mm^{-2}).

All extracellular signals were amplified (×200) and sampled (20 kHz) using a multichannel data acquisition system (Bio-signal Technologies). Data were pre-processed by CED spike2 v7.16 (Cambridge Electronic Design) and Offline sorter v3.3.5 (Plexon). Raw data were band-passed filtered at 3–5,000 Hz, and signals of all trials were averaged for further analysis. Consistent with previous study[19], the VEP amplitude was measured from the maximum and minimum values of the cortical signal during the first 300 ms post stimulus. Noise level was defined as the standard deviation of the signal during the 50 ms preceding this stimulus, and threshold for detectable VEP response was defined as a deviation from the baseline by more than six times the noise level, consistent with previous studies[19,75]. For each grating size, the VEP amplitude was normalized to the maximum amplitude in each animal. We fitted the plot of the normalized VEP amplitude as a function of the stripe width with a second-degree polynomial function and defined the visual acuity limit as the intersection point of the fitted curve with the threshold.

Immunohistochemistry

Mice were deeply anaesthetized using overdose isoflurane for euthanasia and perfused transcardially with 0.9% saline, followed by 4% paraformaldehyde (PFA) using a perfusion pump. For immunohistochemistry of mice brains, the brains were post-fixed in 4% PFA at 4 °C overnight and then dehydrated in 30% sucrose. After being embedded and frozen, brain tissues were sectioned into 30-μm-thick coronal slices in a cryostat (Leica CM1950, Leica). The slices were washed with Tris-buffered saline (TBS) five times (5 min each) and covered with coverslips. Fluorescent images were obtained by fluorescence imaging microscope (A1R, Nikon) and analysed in ImageJ software 1.48v (National Institutes of Health, NIH) and NIS-Elements AR software ver. 4.30.01 (Nikon).

For immunohistochemistry of mouse retinas, eyes were enucleated, and then the retinas were dissected and fixed in 4% PFA for 4–7 h at 4 °C. Then the retinas were dehydrated using 10%, 20% and 30% sucrose solution respectively. After dehydration, the retinas were embedded in optimal cutting temperature compound (OCT) compound at −80 °C for more than 2 h, and subsequently sectioned into 14-μm slices in a cryostat (Leica CM1950, Leica). After being rinsed with TBS and immersed in 0.5% Triton-X-100 for 20 min, slices were incubated in a blocking solution consisting of 10% donkey serum (Jackson Immunoresearch) and 1% bovine serum albumin in 0.05 M TBS for 2 h. Slices were then incubated by primary antibody (anti-PKC-α, Thermo Fisher (MA1-157), 1:200; anti-S opsin and anti-ATP1A3, Abcam (ab235274 and ab182571, respectively), 1:200) diluted in blocking solution overnight. The following day, slices were washed three times (5 min each), and secondary antibody (donkey anti-mouse conjugated to Alexa Flour 647, donkey anti-goat conjugated to Alexa Flour 488, and donkey anti-rabbit conjugated to Alexa Flour 594, Jackson ImmunoResearch, 1:300) diluted in blocking solution was used to cover the slices for 2 h in darkness. Slices were then stained with 1:3,000 DAPI, and finally rinsed, air-dried and mounted. Fluorescent images were obtained by fluorescence imaging microscope (A1R, Nikon) and analysed in ImageJ software 1.48v (NIH) and NIS-Elements AR software ver. 4.30.01 (Nikon).

The immunohistochemistry protocol for whole-mount retinas was similar to that in retina slices. After eye enucleation and retina dissection, retinas were fixed in 4% PFA for 5–7 h at 4 °C. The retinas were washed with TBS and blocked with 10% donkey serum, followed by primary antibody (anti-Brn3a, Santa Cruz Biotechnology (SC-31984), 1:200; anti-PKC-α, Thermo Fisher (MA1-157), 1:200) solution for 24–30 h at 4 °C. After washing in TBS, retinas were transferred to the secondary antibody (donkey anti-goat conjugated to Alexa Flour 594 and anti-mouse conjugated to Alexa Flour 488, Jackson ImmunoResearch, 1:300) solution for 3 h at room temperature in the dark. After being washed, whole-mounted retinas were air dried and mounted by Fluruomount-G (Southern Biotech). Fluorescent images were obtained by fluorescence imaging microscope (Eclipse Ni, Nikon) and confocal multi-photon scanning microscope (AIR-MP, Nikon) and analysed in ImageJ software 1.48v (NIH) and NIS-Elements AR software ver. 4.30.01 (Nikon).

Intravitreal injection in mice

The mice were anaesthetized with isoflurane (1–2% at 0.5–1.0 l min^{-1}). Subsequently, 69 nl DiI Stain Perchlorate (1.5 mg ml^{-1}, D282, Invitrogen) was injected into the dorsal nasal retina of *rd1/cDTA* mice, where the NW arrays were implanted, using a Nanoject II (Drummond Scientific Company). After surgery, eye ointment was applied with a cotton swab, and the mice were placed on a heating pad until fully recovered from anaesthesia.

Stereotaxic injection in mice

The mice were first anaesthetized with isoflurane (1–2% at 0.5–1.0 l min^{-1}). The scalp was shaved, and the mice were placed in a stereotaxic apparatus. Body temperature was maintained using a heating pad. Eye ointment was applied with a cotton swab to keep the mouse's cornea moist. Skin was disinfected with 70% ethanol and betadine, then removed to expose the skull. Cranial drill was used to thin the skull over the injection site, and the AAVs or CTB-488 were injected into V1 through glass pipette using a Nanoject II injector (Drummond Scientific Company). The injection program was 40 pulses of 2.3 nl each (92 nl total volume), at 10-s intervals. The pipette was left in the inject regions for 5 min after injection, and then slowly retracted. Clean the wound area with sterile saline and suture the wound carefully. AAV2/8-hSyn-GCaMP6s (Taitool Bioscience) was delivered to V1, 2.1–2.6 mm laterally and 3.2–3.6 mm posteriorly from Bregma and at a depth of L2/3 (200–400 μm); CTB-488 was delivered to the same region in V1.

Cranial window implantation in mice

Surgery for cranial window implantation was performed 6–8 weeks after virus injections when the mice were over 3.5–4 months old. The craniotomy method and position were the same as those in the VEP experiment. A custom-made glass window (0.1 mm thickness) was embedded into the craniotomy and sealed with VetBond (3M Animal

Care Products). Dental cement (Super Bond C&B) was applied to secured the window. A head bar was finally mounted on the skull using the same dental cement. Mice were given a dose of ceftiofur sodium (5 mg kg^{-1} body weight, Quan Yu Biotechnology Animal Pharmaceutical; intraperitoneal injection), dexamethasone sodium phosphate (0.1 mg kg^{-1} body weight, Quanyu Biotechnology Animal Pharmaceutical; intramuscular injection) at the end of surgery. Animals were placed on a heating pad until fully recovered from anaesthesia, and then transferred back to their home cage.

All mice were allowed to recover in home cage for 2 weeks before imaging. Animals that show overt signs of sickness, infection of the wound, loss of body weight or other signs of reduced wellbeing must undergo special care: for example, an extra dose of analgesics to minimize post-operative pain, and/or a subcutaneous injection of saline to support rehydration.

Procedure for two-photon calcium imaging in mice

Recordings of GCaMP6 fluorescence signals were performed using Olympus FluoView FVMPE-RS upright two-photon laser-scanning system with an Olympus XL Plan N25×/1.05 WMP∞/0-0.23/FN/18 dipping objective (Olympus) and a miniature two-photon microscope (DPHLMTPM-V2.0, Beijing Transcend Vivoscope Biotech). Two-photon excitation was performed using 920 nm MAITAI eHPDS-OL laser (Mai Tai, Spectra-Physics), and emitted fluorescence was detected through a 495–540 nm bandpass filter. For the examination of GCaMP6s signals in V1, cranial window was imaged at a resolution of 512 × 512 pixels at 30 Hz. Imaging sessions lasted 2–3 h including 1–2 h of effective imaging time.

In light-evoked responses experiments, mice were habituated to head fixation and running on the cylindrical treadmill. Once the animals were comfortable with the setup, imaging was performed. The mice were kept awake during imaging. In the experiments of receptive field mapping and natural scenes stimulation, the mice were anaesthetized with isoflurane (0.5–1.0% at 0.5–1.5 l min^{-1}) and placed on a heating pad to maintain body temperature. Sodium hyaluronate eye drops (0.3%) were applied to the eyes to prevent drying.

Visual stimulus for two-photon calcium imaging

Blue LED was used as light source for the light-responsive experiments. LED was located 6 cm away from the animal's eye. Each trial started with a blank period for 20–25 s randomly, and a LED stimulation was subsequently turned on for 1 s and repeated six times.

Visual stimuli used in receptive field mapping were generated by Psychopy toolbox[74]. The screen (28 × 24 cm) was 12 cm away from the eye contralateral to the imaging site. A blue square was flashed on a black background in a 6 × 5 grid in a pseudorandom order; each square is 16 × 16 degrees. The squares were presented for 1 s followed by a 10-s interval, and repeated eight times.

Stimuli of drifting grating were generated by Psychopy toolbox[74]. Drifting gratings in eight directions (0–315°, 45°) appeared in a pseudo-random order with a stimulus duration of 1 s and interval of 8 s. Each direction of stimulus was repeated eight times.

Stimuli of natural scenes were consisted of 30 natural images from the van Hateren Natural Image Dataset[76] and the McGill Calibrated Colour Image Database[77]. The images of 800 × 600 pixels were presented in greyscale with normalized contrast. Each image was presented for 0.5 s followed by 5 s inter-image grey period and repeated four to eight times.

Analysis of in vivo calcium imaging data

In vivo calcium movies were pre-processed in Python using a custom-built pipeline based on CaImAn package (v1.9)[78] for large-scale calcium imaging data analysis. Movies were motion-corrected using a rigid registration method to remove motion artefacts[79]. Fluorescence traces of individual neurons were extracted from the registered movie using a constrained non-negative matrix factorization framework[80]. Spatial correlation thresholds for region of interest detection were set to 0.85, and the signal-to-noise ratio for accepting a component was set to 2.50. The automatic detection was manually screened to ensure correct segmentation of somatic calcium activity. This pipeline generated a set of spatial footprints and temporal traces for each animal on each day of recording. The relative changes in fluorescence ($\Delta F/F$) trace were used in further analyses.

Identification of light-responsive neurons

To identify light-responsive neurons, we defined a pre-stimulus period as the 2-s window (60 frames) preceding the stimulus onset, and the baseline of the trial was the mean $\Delta F/F$ during the pre-stimulus period. We also defined a post-stimulus period as the 5-s window (150 frames) following the stimulus onset. Post-stimulus window was 3 s in the natural scenes stimulus experiments. A neuron was considered responsive to the 1-s light pulses if the maximum $\Delta F/F$ during the post-stimulus period was more than five times standard deviation above the baseline, and the time to decay half-peak must be over ten frames in more than 50% of the trials. In the natural scenes test, the neuron that satisfied the above conditions would be identified as a responsive cell for further analysis.

Mean $\Delta F/F$ amplitude and latency in V1 neurons

To estimate a region of interest's $\Delta F/F$ mean amplitude in response to light stimuli, we segmented the $\Delta F/F$ traces during each light-evoked spiking and used the maximum $\Delta F/F$ value at each segment as a measurement of the $\Delta F/F$ amplitude for that particular segment. The time between the onset of the visual stimuli and the frame at which the $\Delta F/F$ trace first exceeded the threshold was defined as the latency. Mean amplitude and mean latency were the average amplitude and the average latency of all light-responsive neurons, respectively. For each mouse in Fig. 5g, $\Delta F/F$ amplitude was normalized according to the amplitude on the third day after implantation. For each mouse in Fig. 5h, latency was normalized to the mean latency of normal mice.

Fitting spatial receptive fields in V1 neurons in mice

The retinotopic organization of individual neurons was assessed by measuring the average $\Delta F/F$ response to each of the 30 stimulus positions (6 × 5 grid) with eight repetitions. These data were interpolated by a 2D bilinear interpolation, and fit by least-squares regression with a two-dimensional Gaussian model. Neurons whose receptive field (centre) were positioned 5° from the edge of the screen (that provide visual stimuli) were chosen for further analysis.

Lifetime sparseness

Lifetime sparseness was computed from the mean responses to natural scenes by using the definition in previous study[59,60], as

$$S_L = \frac{1 - \frac{1}{N}\frac{(\sum_i r_i)^2}{\sum_i r_i^2}}{1 - \frac{1}{N}} \quad (1)$$

where N is the number of stimulus conditions and r_i is the mean response to stimulus condition i across the test.

Surgical procedures for NW array implantation in monkeys

Macaque monkey was anaesthetized with intramuscular tiletamine hydrochloride and zolazepam hydrochloride (Zoletil 50, 0.1 ml kg^{-1} body weight, Virbac) 20 min after intramuscular atropine (0.5 mg ml^{-1}, 0.1 ml kg^{-1} body weight, Healton Animal Pharmaceutical). Isoflurane inhalation maintained general anaesthesia during retinal implant surgery. Mydriasis was induced by tropicamide (5 mg ml^{-1}, Santen Pharmaceutical). Lateral canthotomy was performed to allow 23-gauge pars plana vitrectomy (Alcon Consellation) for vitrectomy, and a retinal

bleb was created by subretinal injection of balanced salt solution[23]. NW arrays were 1.8 mm in length and 0.4 mm in width, so as to be guided into the eyes through 23-gauge trocars for vitrectomy without an additional incision. NW arrays was then inserted subretinally through 2-mm-wide retinotomy (Constellation Vision System). Eight and six pieces of NW arrays were implanted for monkeys A and E, respectively. The detached retina was re-attached by perfluorocarbon liquid (Bausch & Lomb) and silicone oil (Arciolane3000, Arcadophta SARL). Retinal laser photocoagulation was performed at the border of the retinotomy[81,82].

Eye examinations for macaque monkey

One to two drops of Compound Tropicamide Eye Drops (Santen Pharmaceutical) were instilled into the monkeys' eyes to dilute their pupil three times 1 h before the examination. Monkeys were injected with atropine (0.5 mg ml^{-1}, 0.1 ml kg^{-1} body weight, Healton Animal Pharmaceutical) followed by intramuscular injection of tiletamine hydrochloride and zolazepam hydrochloride (Zoletil 50, 0.1 ml kg^{-1} body weight, Virbac). After anaesthetization, the animal was placed prone in a supporting apparatus to receive eye examinations.

Colour, red-free and autofluorescence fundus photography (TRC-50DX, TOPCON) was taken before photocoagulation, 11 months after photocoagulation, 4 days and 3, 4, 6 and 8 weeks after NW array implantation for monkey A and before implantation, and 2 weeks after implantation for monkey E. OCT (Cirrus HD-OCT 4000, Zeiss) was used to scan the retinal structure and the corresponding places of NW arrays. OCT images were taken at 4 days and 3, 4, 6 and 8 weeks after implantation with NW arrays for monkey A and before implantation and 2 weeks after implantation for monkey E. Silt lamp (Oculus Optikgerate GmbH) was used to examine monkey's lenses, cornea and anterior chamber by providing direct visualization.

Colour fundus photography (AFC-330, NIDEK) and OCT images (Mocean 3000 Plus, Silton Technology) were taken 8, 36, 48 and 54 weeks after NW array implantation for monkey E.

VGS task in monkeys

The monkey was seated in a chair that was placed on a platform in front of the screen (the distance between the monkey's eyes and the screen is 30 cm) and looked flat at the central fixation point. A lightweight acrylic cap was implanted for head stabilization chronically. Monkey's head was fixed by a custom-made head holder to keep the head stable during experiment. Pupil position was monitored and digitalized by an infrared eye system, including an eye-tracking camera (above the centre of the screen), infrared illuminator, Eyelink plus 1000 (SR Research) and Wise Center software (Jisimingzhi Technology).

Visual stimuli were presented by red (642/18 nm), blue (465/25 nm) or UV (360/15 nm) LED, which were generated by TEMPO experiment control system (Reflective Computing), Neurontask software (0.3-pre alpha, SourceForge) and Arduino. Monkey's eye in VGS task was 30 cm away from the stimulus. The light intensity of the stimulus (red (642/18 nm), blue (465/25 nm) or UV (360/15 nm) LED) was set to ~10.00 μW mm^{-2} by an electric current source (DP3005B, MESTEK) at a distance of 30 cm from the stimulus. We also measured the light intensity at a distance of 6 cm (~107.00 μW mm^{-2}) from the same stimulus to ensure consistency with mice experiment.

The monkeys were trained daily to perform a VGS task and rewarded for making a correct saccadic eye movement from a central fixation point (equipped with an LED) to a peripheral target point (equipped with an LED). In each session, stimuli were presented in the implanted region and more than four normal regions in a random order. Up to ten sessions were recorded daily. Once monkeys fixated at the fixation point for 1 s, the LED at the target point was turned on for 1 s while the LED at the fixation point was turned off. The visual field was divided into 36 polar angles, with eccentricity from 17° to 21° (interval 2°). The eye movement data from macaque behavioural experiments were extracted and pre-processed using a customized MATLAB (MathWorks) script for subsequent analysis.

To calculate the saccadic endpoint, we measured the velocity of eye movement trajectories using customized Python code. The saccadic endpoint was the average position in the time window when the eye was first stationary for 50–100 ms after peak velocity[25]. The monkeys were considered to have completed one correct saccade when the animal gaze reached a 15° window surrounding the target point and maintained more than 50 ms. The monkeys were rewarded when they made a correct saccadic eye movement. Each saccadic endpoint was normalized according to the relative position of the target point.

For the VGS task, the velocity was calculated from the trace of eye movement. The period of fixation was defined as the period of baseline. Saccade onset was defined as the velocity of saccade was more than two times standard deviation above the baseline. The saccade latency was defined as the time from the target point stimuli onset to the saccade onset. The data of the correct trials were used for the calculation of mean saccade latency.

MP exposure for ocular safety

The maximum permissible (MP) exposure for ocular safety as ANSI 2000 (ref. 34) was calculated as below. The parameters to generate the MP exposures for ocular safety in the electrophysiological experiments are listed in Supplementary Table 4. For stimuli wavelength between 400 nm and 600 nm, the parameters used to calculate the MP exposures for ocular safety were identical. If the original parameter was a range, the value with this range that minimizes MP exposures would be employed in the calculation. Following the ANSI standard for ophthalmic applications and for repetitive pulses, only MP average radiant powers entering the natural or dilated pupil ($MP\Phi_{av}$) were included. $MP\Phi_{av,2}$ and $MP\Phi_{av,3}$ the radiant power of the stimulus was safe under the ANSI 2000 standard[34]. The detailed calculation steps were as follows.

Rule 2 (photochemical limit): this limit is that of the continuous exposure injury of duration $T = 20$ s (C_B, function of stimulation wavelength as defined in the ANSI standard):

$$\begin{aligned} MP\Phi_{av,2} &= MP\Phi[T] = 5.56 \times 10^{-6} C_B \alpha^2 T^{-1} \\ &= 5.56 \times 10^{-6} \times 1 \times 10.76^2 \times 20^{-1} \\ &= 31.91\,\mu W \end{aligned} \quad (2)$$

Rule 3: this limit is that of the subthreshold pulse-cumulative thermal injury by any single pulse within a group of pulses (C_T, function of stimulation wavelength as defined in the ANSI standard. C_E, function of angular subtense of source as defined in the ANSI standard):

$$\begin{aligned} MP\Phi_{av,3} &= n^{-0.25}\delta MP\Phi[t_1] \\ &= n^{-0.25}\delta \times \{6.93 \times 10^{-4} C_T C_E(t_1)^{-0.25}\} \\ &= 10^{-0.25} \times 0.0125 \times \{\, 6.93 \times 10^{-4} \times 1 \times \\ &\quad (0.667 \times 10.76) \times 0.025^{-0.25} \\ &= 87.54\,\mu W \end{aligned} \quad (3)$$

Statistics and reproducibility

No statistical methods were used to pre-determine sample sizes. Sample sizes were determined by the number of biological replicates that are necessary for ensuring statistical significance, and our sample sizes are similar to those reported in previous publications[4,6,25]. The differences and normality for multiple comparisons were tested by SigmaPlot v12.5 (SYSTAT) and Prism v9.5 (GraphPad). Comparisons between two distinct samples were made by two-tailed Student's unpaired *t*-test, and paired *t*-test was used for data with repeated measurements from the same sample. Comparisons between three or more distinct samples

were made by one-way analysis of variance (ANOVA) followed by the Tukey post-hoc test. Results of the choice-box-based behavioural test were analysed by two-way repeated-measures (RM) ANOVA followed by the Tukey post-hoc test. With regard to the fitting model, we used log-linear regression to fit the data. $P < 0.05$ was considered statistically significant. All data are expressed as mean ± standard error of the mean (s.e.m.) or as individual plots. Full statistical analyses corresponding to each figure can be found in Supplementary Table 3.

Figure 1b,c showed the fraction of response with different pulse durations and light intensities in different experiments, respectively. The fraction of response in Fig. 1c reflects the number of trials that evoked cell response among all trials. The normalized cell response in Fig. 1d reflects the relative firing rate of cells. The same rationale applies to Fig. 2c,d. Figure 4h,k shows the percentage of orientation- and direction-selective cells for the same data, respectively. In Fig. 7f,i, the left panel shows the correct rate at different light intensities, while the right panel shows the correct rate under maximum light intensity.

Due to the common practice that ophthalmic examinations yield one representative image at one specific timepoint, Fig. 6a–f shows representative images from one experiment at each timepoint.

Reporting summary

Further information on research design is available in the Nature Portfolio Reporting Summary linked to this article.

Data availability

The raw and analysed datasets generated during the study are available for research purposes from the corresponding authors on reasonable request. The study using stimuli of natural scenes used 30 natural images from the van Hateren Natural Image Dataset (https://github.com/hunse/vanhateren) and the McGill Calibrated Colour Image Database (http://tabby.vision.mcgill.ca.). Source data are provided with this paper.

Code availability

Custom-written codes used to analyse data from this study are available from the corresponding authors on request.

References

1. Maguire, A. M. et al. Safety and efficacy of gene transfer for Leber's congenital amaurosis. *N. Engl. J. Med.* **358**, 2240–2248 (2008).
2. Cascella, R. et al. Towards the application of precision medicine in age-related macular degeneration. *Prog. Retin. Eye Res.* **63**, 132–146 (2018).
3. Zhou, H. et al. Glia-to-neuron conversion by CRISPR–CasRx alleviates symptoms of neurological disease in mice. *Cell* **181**, 590–603 (2020).
4. Mahato, B. et al. Pharmacologic fibroblast reprogramming into photoreceptors restores vision. *Nature* **581**, 83–88 (2020).
5. Hoang, T. et al. Gene regulatory networks controlling vertebrate retinal regeneration. *Science* **370**, eabb8598 (2020).
6. Lu, Y. et al. Reprogramming to recover youthful epigenetic information and restore vision. *Nature* **588**, 124–129 (2020).
7. Maeder, M. L. et al. Development of a gene-editing approach to restore vision loss in Leber congenital amaurosis type 10. *Nat. Med.* **25**, 229–233 (2019).
8. Sahel, J. A. et al. Partial recovery of visual function in a blind patient after optogenetic therapy. *Nat. Med.* **27**, 1223–1229 (2021).
9. Roska, B. & Sahel, J. A. Restoring vision. *Nature* **557**, 359–367 (2018).
10. Sahel, J. A., Bennett, J. & Roska, B. Depicting brighter possibilities for treating blindness. *Sci. Transl. Med.* **11**, eaax2324 (2019).
11. Humayun, M. S. et al. Visual perception elicited by electrical stimulation of retina in blind humans. *Arch. Ophthalmol.* **114**, 40–46 (1996).
12. da Cruz, L. et al. Five-year safety and performance results from the argus ii retinal prosthesis system clinical trial. *Ophthalmology* **123**, 2248–2254 (2016).
13. Wilke, R. et al. Spatial resolution and perception of patterns mediated by a subretinal 16-electrode array in patients blinded by hereditary retinal dystrophies. *Invest. Ophthalmol. Vis. Sci.* **52**, 5995–6003 (2011).
14. Mills, J. O., Jalil, A. & Stanga, P. E. Electronic retinal implants and artificial vision: journey and present. *Eye* **31**, 1383–1398 (2017).
15. Stingl, K. et al. Interim results of a multicenter trial with the new electronic subretinal implant alpha AMS in 15 patients blind from inherited retinal degenerations. *Front. Neurosci.* **11**, 445 (2017).
16. Edwards, T. L. et al. Assessment of the electronic retinal implant alpha ams in restoring vision to blind patients with end-stage retinitis pigmentosa. *Ophthalmology* **125**, 432–443 (2018).
17. Palanker, D., Le Mer, Y., Mohand-Said, S., Muqit, M. & Sahel, J. A. Photovoltaic restoration of central vision in atrophic age-related macular degeneration. *Ophthalmology* **127**, 1097–1104 (2020).
18. Palanker, D., Le Mer, Y., Mohand-Said, S. & Sahel, J. A. Simultaneous perception of prosthetic and natural vision in AMD patients. *Nat. Commun.* **13**, 513 (2022).
19. Lorach, H. et al. Photovoltaic restoration of sight with high visual acuity. *Nat. Med.* **21**, 476–482 (2015).
20. Wang, B. Y. et al. Electronic photoreceptors enable prosthetic visual acuity matching the natural resolution in rats. *Nat. Commun.* **13**, 6627 (2022).
21. Huang, T. W. et al. Vertical-junction photodiodes for smaller pixels in retinal prostheses. *J. Neural Eng.* **18**, 036015 (2021).
22. Ho, E. et al. Temporal structure in spiking patterns of ganglion cells defines perceptual thresholds in rodents with subretinal prosthesis. *Sci. Rep.* **8**, 3145 (2018).
23. Prevot, P. H. et al. Behavioural responses to a photovoltaic subretinal prosthesis implanted in non-human primates. *Nat. Biomed. Eng.* **4**, 172–180 (2020).
24. Beauchamp, M. S. et al. Dynamic stimulation of visual cortex produces form vision in sighted and blind humans. *Cell* **181**, 774–783 (2020).
25. Chen, X., Wang, F., Fernandez, E. & Roelfsema, P. R. Shape perception via a high-channel-count neuroprosthesis in monkey visual cortex. *Science* **370**, 1191–1196 (2020).
26. Gu, L. et al. A biomimetic eye with a hemispherical perovskite nanowire array retina. *Nature* **581**, 278–282 (2020).
27. Nelidova, D. et al. Restoring light sensitivity using tunable near-infrared sensors. *Science* **368**, 1108–1113 (2020).
28. Maya-Vetencourt, J. F. et al. Subretinally injected semiconducting polymer nanoparticles rescue vision in a rat model of retinal dystrophy. *Nat. Nanotechnol.* **15**, 698–708 (2020).
29. Acaron Ledesma, H. et al. An atlas of nano-enabled neural interfaces. *Nat. Nanotechnol.* **14**, 645–657 (2019).
30. Tang, J. et al. Nanowire arrays restore vision in blind mice. *Nat. Commun.* **9**, 786 (2018).
31. Li, J. et al. Nanoscale stacking fault-assisted room temperature plasticity in flash-sintered TiO_2. *Sci. Adv.* **5**, eaaw5519 (2019).
32. Wang, G., Wang, H., Ling, Y., Tang, Y. & Li, Y. Hydrogen-treated TiO_2 nanowire arrays for photoelectrochemical water splitting. *Nano Lett.* **11**, 3026–3033 (2011).
33. Stirman, J., Townsend, L. B. & Smith, S. A touchscreen based global motion perception task for mice. *Vis. Res* **127**, 74–83 (2016).
34. Delori, F. C., Webb, R. H., Sliney, D. H., & American National Standards Institute. Maximum permissible exposures for ocular safety (ANSI 2000), with emphasis on ophthalmic devices. *J. Opt. Soc. Am. A* **24**, 1250–1265 (2007).

35. Goetz, G. A. & Palanker, D. V. Electronic approaches to restoration of sight. *Rep. Prog. Phys.* **79**, 096701 (2016).
36. Xiong, Y.-Z. et al. Relationship between acuity and contrast sensitivity: differences due to eye disease. *Invest. Ophthalmol. Vis. Sci.* **61**, 40–40 (2020).
37. Schmucker, C. & Schaeffel, F. In vivo biometry in the mouse eye with low coherence interferometry. *Vis. Res* **44**, 2445–2456 (2004).
38. Ganjawala, T. H., Lu, Q., Fenner, M. D., Abrams, G. W. & Pan, Z. H. Improved CoChR variants restore visual acuity and contrast sensitivity in a mouse model of blindness under ambient light conditions. *Mol. Ther.* **27**, 1195–1205 (2019).
39. Prusky, G. T., West, P. W. & Douglas, R. M. Behavioral assessment of visual acuity in mice and rats. *Vis. Res* **40**, 2201–2209 (2000).
40. Sinex, D. G., Burdette, L. J. & Pearlman, A. L. A psychophysical investigation of spatial vision in the normal and reeler mutant mouse. *Vis. Res* **19**, 853–857 (1979).
41. Prusky, G. T., Alam, N. M., Beekman, S. & Douglas, R. M. Rapid quantification of adult and developing mouse spatial vision using a virtual optomotor system. *Invest. Ophthalmol. Vis. Sci.* **45**, 4611–4616 (2004).
42. Tomita, H. et al. Channelrhodopsin-2 gene transduced into retinal ganglion cells restores functional vision in genetically blind rats. *Exp. Eye Res* **90**, 429–436 (2010).
43. Histed, M. H., Carvalho, L. A. & Maunsell, J. H. Psychophysical measurement of contrast sensitivity in the behaving mouse. *J. Neurophysiol.* **107**, 758–765 (2012).
44. Harvey, B. M. & Dumoulin, S. O. The relationship between cortical magnification factor and population receptive field size in human visual cortex: constancies in cortical architecture. *J. Neurosci.* **31**, 13604–13612 (2011).
45. Wang, Q. & Burkhalter, A. Area map of mouse visual cortex. *J. Comp. Neurol.* **502**, 339–357 (2007).
46. Sterratt, D. C., Lyngholm, D., Willshaw, D. J. & Thompson, I. D. Standard anatomical and visual space for the mouse retina: computational reconstruction and transformation of flattened retinae with the Retistruct package. *PLoS Comput. Biol.* **9**, e1002921 (2013).
47. Roth, M. M. et al. Thalamic nuclei convey diverse contextual information to layer 1 of visual cortex. *Nat. Neurosci.* **19**, 299–307 (2016).
48. Samonds, J. M., Feese, B. D., Lee, T. S. & Kuhlman, S. J. Nonuniform surround suppression of visual responses in mouse V1. *J. Neurophysiol.* **118**, 3282–3292 (2017).
49. Schrater, P. R., Knill, D. C. & Simoncelli, E. P. Mechanisms of visual motion detection. *Nat. Neurosci.* **3**, 64–68 (2000).
50. Fisher, Y. E., Silies, M. & Clandinin, T. R. Orientation selectivity sharpens motion detection in *Drosophila*. *Neuron* **88**, 390–402 (2015).
51. Galletti, C. & Fattori, P. Neuronal mechanisms for detection of motion in the field of view. *Neuropsychologia* **41**, 1717–1727 (2003).
52. Wei, W. Neural mechanisms of motion processing in the mammalian retina. *Annu. Rev. Vis. Sci.* **4**, 165–192 (2018).
53. Huang, X. et al. Visual stimulation induces distinct forms of sensitization of On–Off direction-selective ganglion cell responses in the dorsal and ventral retina. *J. Neurosci.* **42**, 4449–4469 (2022).
54. Henschke, J. U. et al. Reward association enhances stimulus-specific representations in primary visual cortex. *Curr. Biol.* **30**, 1866–1880 (2020).
55. Perez-Ortega, J., Alejandre-Garcia, T. & Yuste, R. Long-term stability of cortical ensembles. *eLife* **10**, e64449 (2021).
56. Gdalyahu, A. et al. Associative fear learning enhances sparse network coding in primary sensory cortex. *Neuron* **75**, 121–132 (2012).
57. Kalia, A. et al. Development of pattern vision following early and extended blindness. *Proc. Natl Acad. Sci. USA* **111**, 2035–2039 (2014).
58. Rolls, E. T. & Tovee, M. J. Sparseness of the neuronal representation of stimuli in the primate temporal visual cortex. *J. Neurophysiol.* **73**, 713–726 (1995).
59. Vinje, W. E. & Gallant, J. L. Sparse coding and decorrelation in primary visual cortex during natural vision. *Science* **287**, 1273–1276 (2000).
60. de Vries, S. E. J. et al. A large-scale standardized physiological survey reveals functional organization of the mouse visual cortex. *Nat. Neurosci.* **23**, 138–151 (2020).
61. Kalloniatis, M., Nivison-Smith, L., Chua, J., Acosta, M. L. & Fletcher, E. L. Using the rd1 mouse to understand functional and anatomical retinal remodelling and treatment implications in retinitis pigmentosa: a review. *Exp. Eye Res.* **150**, 106–121 (2016).
62. Spoerl, E., Mrochen, M., Sliney, D., Trokel, S. & Seiler, T. Safety of UVA-riboflavin cross-linking of the cornea. *Cornea* **26**, 385–389 (2007).
63. Watanabe, Y. et al. Development of an optogenetic gene sensitive to daylight and its implications in vision restoration. *NPJ Regen. Med.* **6**, 64 (2021).
64. Stingl, K. et al. Artificial vision with wirelessly powered subretinal electronic implant alpha-IMS. *Proc. Biol. Sci.* **280**, 20130077 (2013).
65. Goo, Y. S. et al. Spontaneous oscillatory rhythm in retinal activities of two retinal degeneration (rd1 and rd10) mice. *Korean J. Physiol. Pharm.* **15**, 415–422 (2011).
66. Stutzki, H., Helmhold, F., Eickenscheidt, M. & Zeck, G. Subretinal electrical stimulation reveals intact network activity in the blind mouse retina. *J. Neurophysiol.* **116**, 1684–1693 (2016).
67. Ahn, J. et al. Correlated activity in the degenerate retina inhibits focal response to electrical stimulation. *Front. Cell Neurosci.* **16**, 889663 (2022).
68. Foik, A. T. et al. Detailed visual cortical responses generated by retinal sheet transplants in rats with severe retinal degeneration. *J. Neurosci.* **38**, 10709–10724 (2018).
69. Muralidharan, M. et al. Neural activity of functionally different retinal ganglion cells can be robustly modulated by high-rate electrical pulse trains. *J. Neural Eng.* **17**, 045013 (2020).
70. Kasi, H. et al. Simulations to study spatial extent of stimulation and effect of electrode–tissue gap in subretinal implants. *Med. Eng. Phys.* **33**, 755–763 (2011).
71. Linderholm, P. et al. Long-term in vivo impedance changes of subretinal microelectrodes implanted in dystrophic P23H rats. *Int. J. Artif. Organs* **36**, 612–619 (2013).
72. Boinagrov, D. et al. Upper threshold of extracellular neural stimulation. *J. Neurophysiol.* **108**, 3233–3238 (2012).
73. Li, X. et al. Serotonin receptor 2c-expressing cells in the ventral CA1 control attention via innervation of the Edinger–Westphal nucleus. *Nat. Neurosci.* **21**, 1239–1250 (2018).
74. Peirce, J. W. PsychoPy—Psychophysics software in Python. *J. Neurosci. Methods* **162**, 8–13 (2007).
75. Ho, E. et al. Characteristics of prosthetic vision in rats with subretinal flat and pillar electrode arrays. *J. Neural Eng.* **16**, 066027 (2019).
76. van Hateren, J. H. & van der Schaaf, A. Independent component filters of natural images compared with simple cells in primary visual cortex. *Proc. Biol. Sci.* **265**, 359–366 (1998).
77. Olmos, A. & Kingdom, F. A. A biologically inspired algorithm for the recovery of shading and reflectance images. *Perception* **33**, 1463–1473 (2004).
78. Giovannucci, A. et al. CaImAn an open source tool for scalable calcium imaging data analysis. *eLife* **8**, e38173 (2019).

79. Pnevmatikakis, E. A. & Giovannucci, A. NoRMCorre: an online algorithm for piecewise rigid motion correction of calcium imaging data. *J. Neurosci. Methods* **291**, 83–94 (2017).
80. Pnevmatikakis, E. A. et al. Simultaneous denoising, deconvolution, and demixing of calcium imaging data. *Neuron* **89**, 285–299 (2016).
81. Matsuo, T. et al. Visual evoked potential recovery by subretinal implantation of photoelectric dye-coupled thin film retinal prosthesis in monkey eyes with macular degeneration. *Artif. Organs* **42**, E186–E203 (2018).
82. Tu, H. Y. et al. Medium- to long-term survival and functional examination of human iPSC-derived retinas in rat and primate models of retinal degeneration. *EBioMedicine* **39**, 562–574 (2019).

Acknowledgements

This work was supported by the MOST of China (2022ZD0208604 and 2022ZD0208605 to J.Z.; 2022ZD0210000 to B.Y.), NSF of China (31771195, 81790640, 81773513 and 820712002 to J.Z.; 32100803 to B.Y.), Shanghai Municipal Science and Technology Major Project (no. 2018SHZDZX01 to J.Z.) and ZJLab, the Key Research and Development Program of Ningxia (no. 2022BEG02046 to J.Z.), Sanming Project of Medicine in Shenzhen (SZSM202011015) to J.Z., Key Scientific Technological Innovation Research Project by Ministry of Education to J.Z., Research and Development Fund of Zhongshan Hospital (2020ZSFZ19 to Y.Y.).

Author contributions

J.Z., B.Y. and Y.Y. conceived the study. J.Z. and B.Y. wrote the paper. R.Y. performed the behavioural experiments of mice and monkeys, performed ex vivo patch-clamp experiments, refined the techniques and analysed the data, with help from P.Z., Z.W, K.S., X.C. and T.Z. C.P. and G.Z. synthesized the $AuTiO_{2-x}$ NW arrays. P.Z., R.Y. and Y.C. developed two-photon microscope setups and chronic calcium imaging. R.Y., X.C., T.Z. and S.W. cut and polished the $AuTiO_{2-x}$ NW arrays. Q.C., L.L., Chengyong J. and G.W. analysed the VEP data. Z.W., Shanshan J., J.L., Z.Y., S.W. and G.W. performed data analysis about patch-clamp experiments. L.W., M.S., C.D., Y.L., X.Z., X.M., Chunhui J. and Y.Y. conducted the surgical procedures for NW array implantation in monkey. C.F., Y.L, Y.W., Y.Z., A.C., F.Z., F.W., Su J. and W.X. worked on monkeys' eyes examinations. All authors discussed the results and commented on the manuscript.

Competing interests

The authors declare no competing interests.

Additional information

Extended data is available for this paper at https://doi.org/10.1038/s41551-023-01137-8.

Supplementary information The online version contains supplementary material available at https://doi.org/10.1038/s41551-023-01137-8.

Correspondence and requests for materials should be addressed to Chunhui Jiang, Yuanzhi Yuan, Biao Yan or Jiayi Zhang.

Peer review information *Nature Biomedical Engineering* thanks the anonymous reviewer(s) for their contribution to the peer review of this work.

Reprints and permissions information is available at www.nature.com/reprints.

Publisher's note Springer Nature remains neutral with regard to jurisdictional claims in published maps and institutional affiliations.

[1]State Key Laboratory of Medical Neurobiology, MOE Frontiers Center for Brain Science, Institutes of Brain Science, Institute for Medical and Engineering Innovation, Department of Ophthalmology, Eye & ENT Hospital, Fudan University, Shanghai, P. R. China. [2]Department of Ophthalmology, Zhongshan Hospital, Fudan University, Shanghai, P. R. China. [3]Laboratory of Advanced Materials, Department of Chemistry, Fudan University, Shanghai, P. R. China. [4]Key Laboratory of Brain Functional Genomics (Ministry of Education), East China Normal University, Shanghai, P. R. China. [5]Shanghai Key Lab for Future Computing Hardware and System, School of Microelectronics, Fudan University, Shanghai, P. R. China. [6]School of Computer Science, Institute for Artificial Intelligence, Peking University, Beijing, P.R. China. [7]School of Computer Science, University of Birmingham, Birmingham, UK. [8]Department of Hand Surgery, the National Clinical Research Center for Aging and Medicine, Huashan Hospital, Fudan University, Shanghai, P. R. China. [9]Department of Hand and Upper Extremity Surgery, Jing'an District Central Hospital, Fudan University, Shanghai, P.R. China. [10]Center of Brain Sciences, Beijing Institute of Basic Medical Sciences, Beijing, P. R. China. [11]Zhongshan Hospital (Xiamen), Fudan University, Xiamen, P.R. China. ✉e-mail: chhjiang70@163.com; yuan.yuanzhi@zs-hospital.sh.cn; biaoyan@fudan.edu.cn; jiayizhang@fudan.edu.cn

https://doi.org/10.1038/s41551-023-01137-8

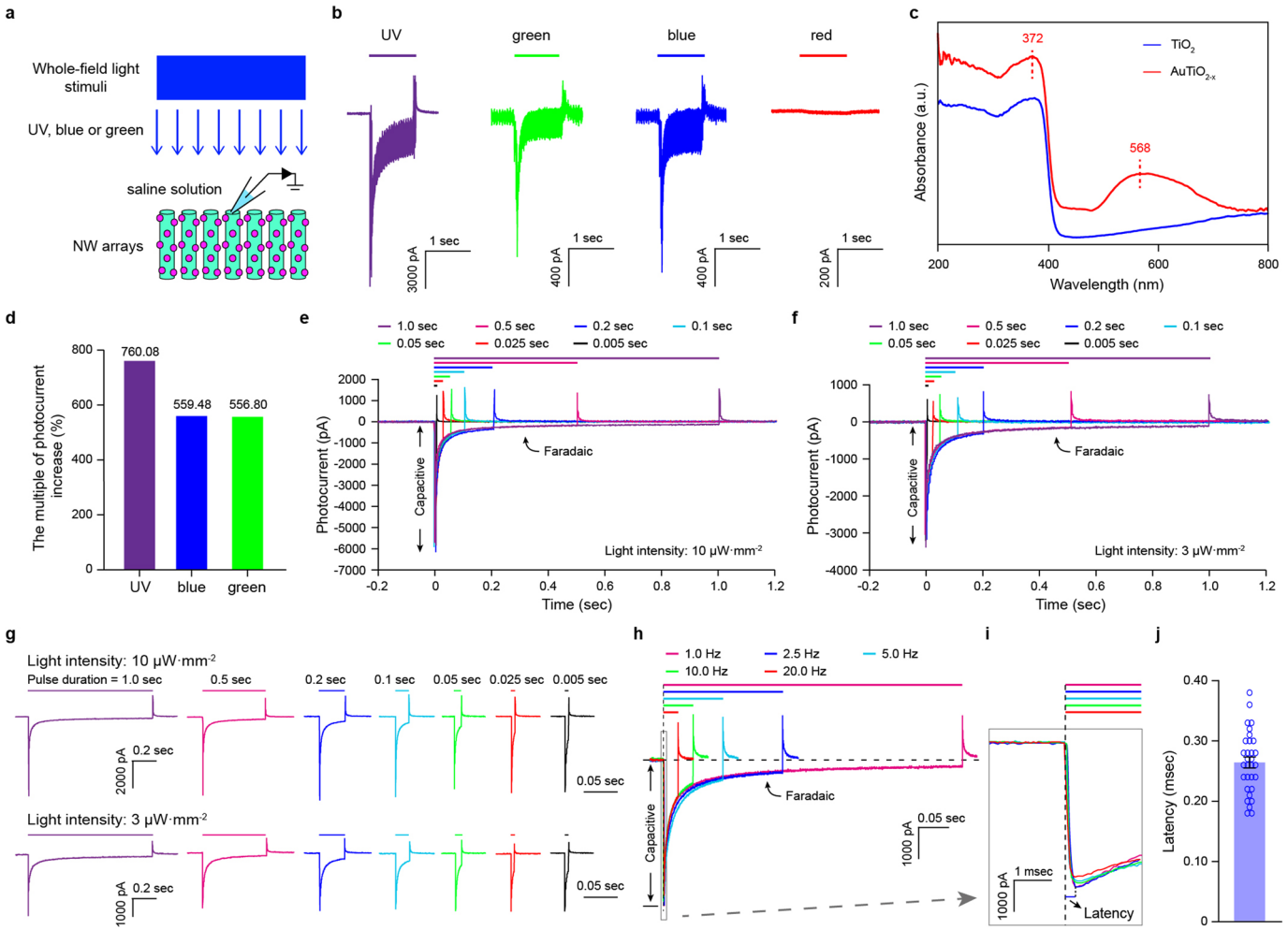

Extended Data Fig. 1 | Characterization of the photocurrent in $AuTiO_{2-x}$ NW arrays. a, Schematic of $AuTiO_{2-x}$ NW arrays photocurrent measurement with UV (375/28 nm, 292.99 μW·mm^{-2}), blue (470/20 nm, 318.47 μW·mm^{-2}) or green (546/12 nm, 420.38 μW·mm^{-2}). The photocurrents were measured by Ag/AgCl electrodes attached to the surface of the NW arrays in normal saline solution. **b**, Photocurrents generated by illumination of UV, blue, green and red light, receptively with an $AuTiO_{2-x}$ NW arrays. **c**, UV-visible absorbance spectra of original TiO_2 and $AuTiO_{2-x}$. **d**, Compared with the published results[30], the photocurrent of improved NW arrays increased by 760.08%, 559.48% and 556.80% under UV, blue and green light, receptively. **e**,**f**, Example of photocurrent measures obtained with UV light stimulus (DMD, wavelength: 400 nm) at 10 μW·mm^{-2} (**e**) and 3 μW·mm^{-2} (**f**) for 0.005–1.0 sec pulse duration. **g**, Photocurrent at 10 μW·mm^{-2} (top) and 3 μW·mm^{-2} (bottom) for 1.0, 0.5, 0.2, 0.1, 0.05, 0.025 and 0.005 sec in **e** and **f**. **h**, Representative photocurrent recording with UV stimulus (DMD, wavelength: 400 nm, light intensity: 10 μW·mm^{-2}) at different flicker frequency (Magenta, 1.0 Hz; blue, 2.5 Hz; cyan, 5.0 Hz; green, 10.0 Hz; red, 20 Hz). **i**, Zoom in photocurrent of gray rectangle in **h**. Dashed black line indicate the stimuli on. **j**, Mean latency of NW arrays to light stimulus (n = 31 measurements from 4 NW arrays). Latency was defined as the time difference between the onset of the visual stimuli and the time that photocurrent reaches the peak value. All data are expressed as mean ± SEM.

https://doi.org/10.1038/s41551-023-01137-8

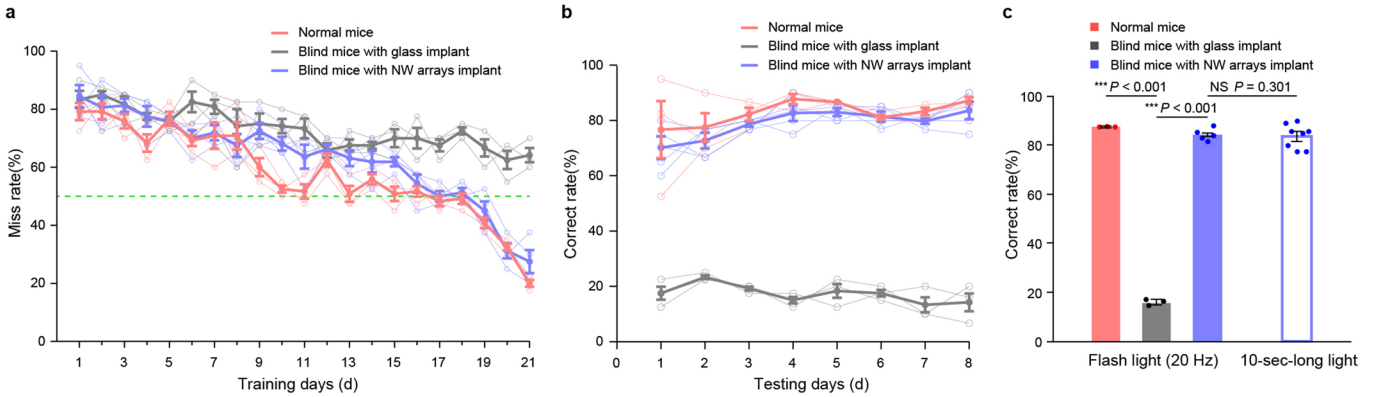

Extended Data Fig. 2 | Miss rate of training trials and choice-box-based light localization test with flashing light at 20 Hz flicker frequency. a, Miss rates of normal mice (red, n = 3 mice), blind mice with glass implant (black, n = 3 mice) and blind mice with NW arrays implant (blue, n = 4 mice) during training trials. Green line indicates 50% miss rate. **b**, Correct rates of normal mice (n = 3 mice), blind mice with glass implant (n = 3 mice) and blind mice with NW arrays-implanted (n = 5 mice) in the choice-box-based behavioural test of light localization with flashing light at 20 Hz flicker frequency (pulse duration: 25 msec). **c**, Correct rates of normal mice (85.02%, red, n = 3 mice), blind mice with glass implant (15.68%, black, n = 3 mice) and blind mice with NW arrays implant (82.07%, blue, n = 5 mice). The correct rates of blind mice with NW arrays implant had no significant difference between flash light at 20 Hz flicker frequency lasted for 10 sec (filled blue column) and 10-sec-long light (hollow blue column). All data are expressed as mean ± SEM. Statistical significance was determined using one-way ANOVA with Tukey's multiple comparisons in **c** (flash light), and two-sided unpaired t-test in **c** (10-sec-long light). NS non-significant. *** $P < 0.001$.

https://doi.org/10.1038/s41551-023-01137-8

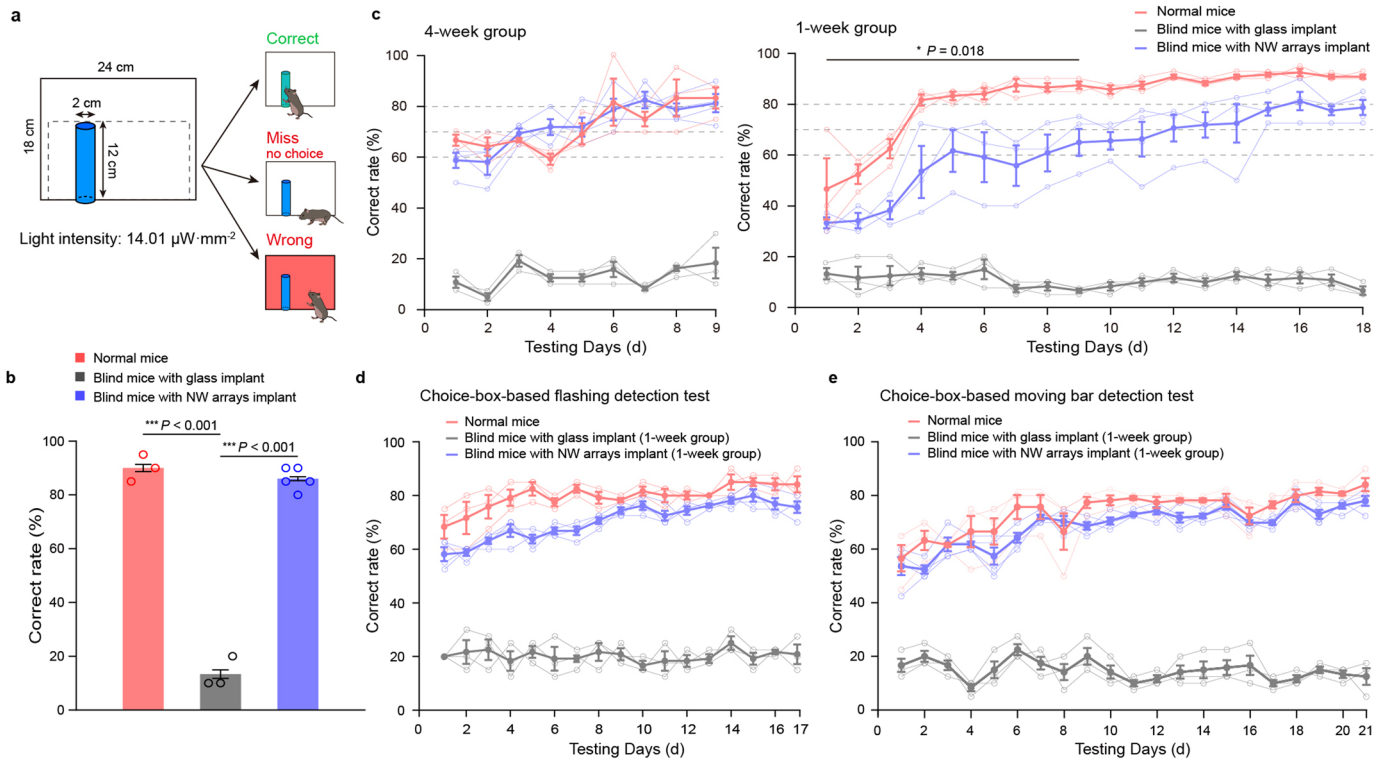

Extended Data Fig. 3 | Choice-box-based static object discrimination test, light localization test, flashing detection test and moving bar detection test of blind mice with the NW arrays implant. a, Schematic of static object discrimination test. Black dashed line indicates the range where the object was placed. **b**, Correct rate of normal mice (red, n = 3 mice), blind mice with glass implant (n = 3 mice) and blind mice with NW arrays implant (n = 5 mice). **c**, Correct rate of 4-week group and 1-week group in choice-box-based light localization test using a UV LED (375/15 nm, 6.24 μW·mm^{-2}). **d**, Correct rates of normal mice (n = 3 mice), blind mice with glass implant (n = 3 mice) and blind mice with NW arrays implant for 1 week (n = 4 mice) in the choice-box-based behavioural test using flashing light. **e**, Correct rates of normal mice (n = 3 mice), blind mice with glass implant (n = 3 mice) and blind mice with NW arrays implant for 1 week (n = 4 mice) in the choice-box-based behavioural test using moving light bars (5.25 degrees, 7.85 degrees/sec, 13.38 μW·mm^{-2}). All data are expressed as mean ± SEM. Statistical significance was determined using one-way ANOVA with Tukey's multiple comparisons in **b**, two-way RM ANOVA with Tukey's multiple comparisons in **c**. * $P < 0.05$, *** $P < 0.001$.

https://doi.org/10.1038/s41551-023-01137-8

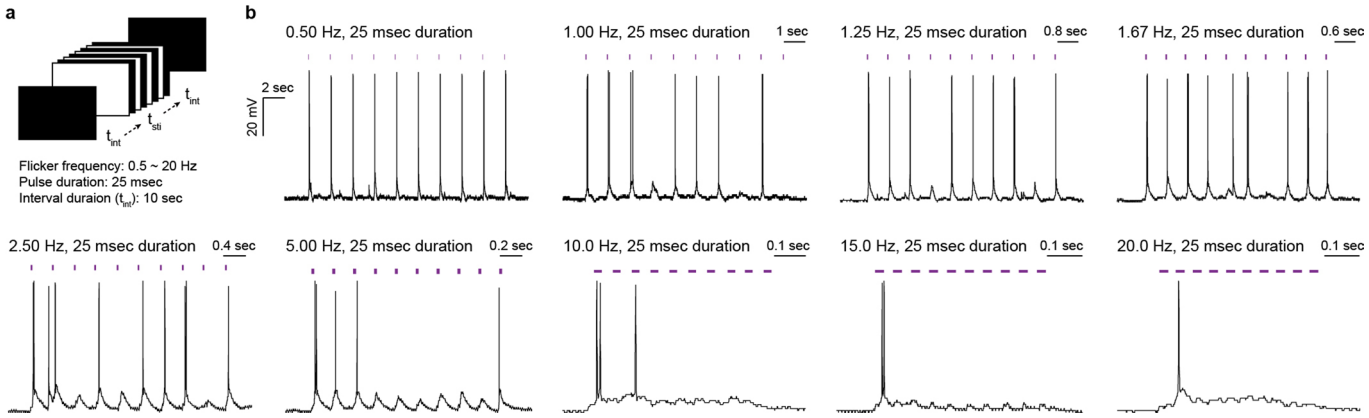

Extended Data Fig. 4 | Responses of RGCs to flashing light in the normal retina. a, Schematic of flashing light stimuli. **b**, Examples responses of RGC to flashing light stimuli in normal retina (Temporal frequency: 0.50-20.0 Hz).

https://doi.org/10.1038/s41551-023-01137-8

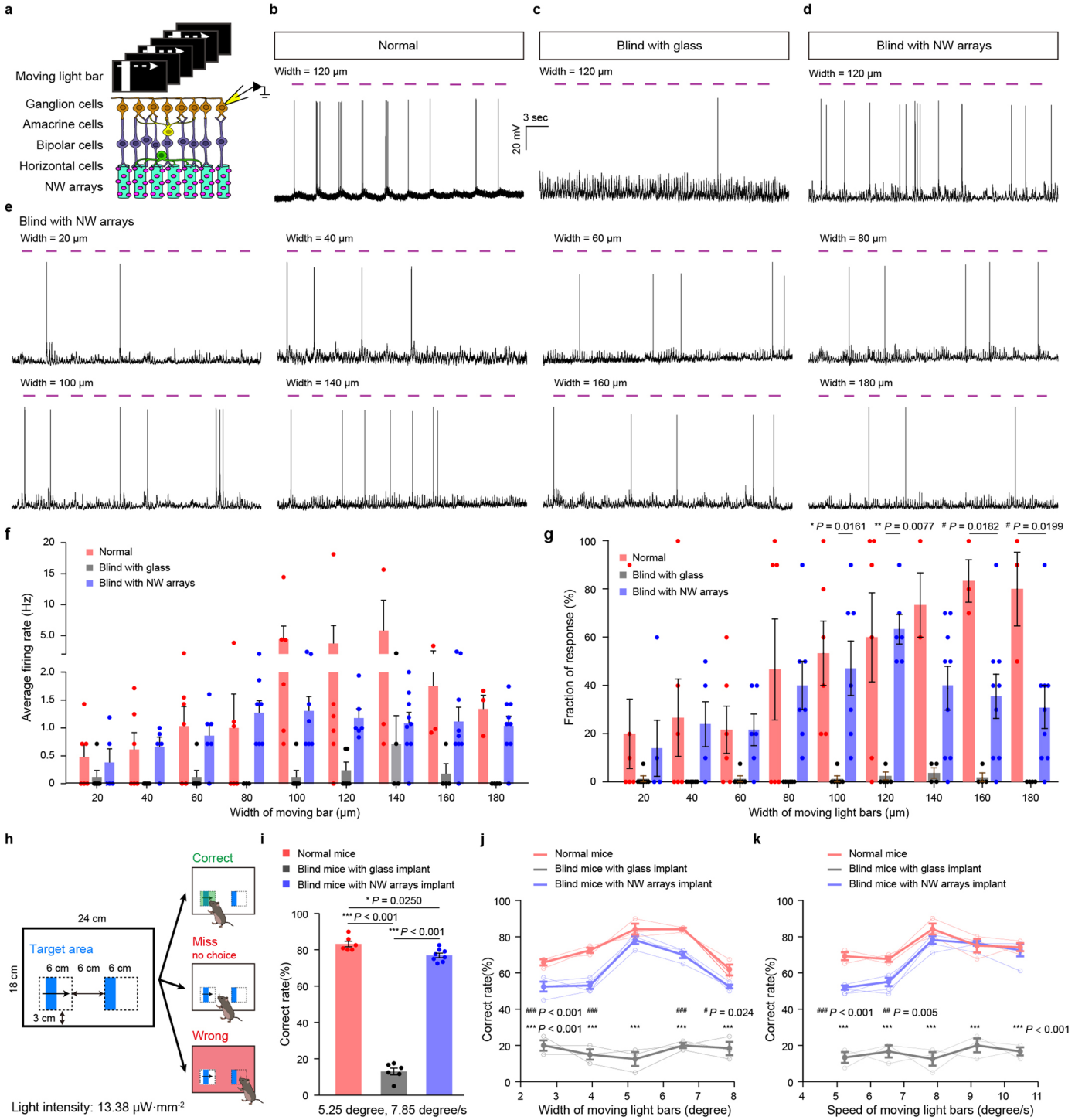

Extended Data Fig. 5 | Responses of RGCs to moving light bars in NW arrays-attached blind retina *ex vivo*, and choice-box-based behavioural test using moving light bars. a, Schematics of *ex vivo* patch-clamp recording with moving light bars stimuli. **b-d**, Responses of representative RGCs to moving light bars stimulus (DMD, wavelength: 400 nm, light intensity: 10 μW·mm^{-2}, width: 120 μm, speed: 200 μm/sec) in normal, blind and NW-array-attached blind retinas. **e**, Responses of a representative RGC to moving light bars stimuli with different width (width: 20–180 μm). **f-g**, Average firing rates and fraction of responses of RGCs in normal (n = 9 RGCs from 6 retinas), blind (n = 10 RGCs from 8 retinas) and NW-array-attached blind retinas (16 RGCs from 10 retinas) using moving light bars with width ranging from 0.64 to 5.76 degrees. **h**, Schematics of the choice-box-based moving bar detection test using moving and static light bar stimuli. **i**, Correct rate of normal mice (n = 6 mice), blind mice with glass implant (n = 6 mice) and blind mice with NW arrays implant (n = 8 mice) in moving bar detection test (5.25 degrees in width at 7.85 degrees/sec). **j-k**, Correct rate of normal mice (n = 3 mice), blind mice with glass implant (n = 3 mice) and blind mice with NW arrays implant (n = 4 mice) in moving bar detection test with moving light bars of different widths and speeds (width: 2.63–7.88 degrees, speed: 5.23–10.47 degrees/sec). All data are expressed as mean ± SEM. Statistical significance was determined using one-way ANOVA with Tukey's multiple comparisons in **g** and **i**, two-way RM ANOVA with Tukey's multiple comparisons in **j** and **k**. * indicates a significant difference between blind mice with NW arrays and blind mice with glass implant, # indicates a significant difference between blind mice with NW arrays and normal mice. * and # $P < 0.05$, ** and ## $P < 0.01$, *** $P < 0.001$.

https://doi.org/10.1038/s41551-023-01137-8

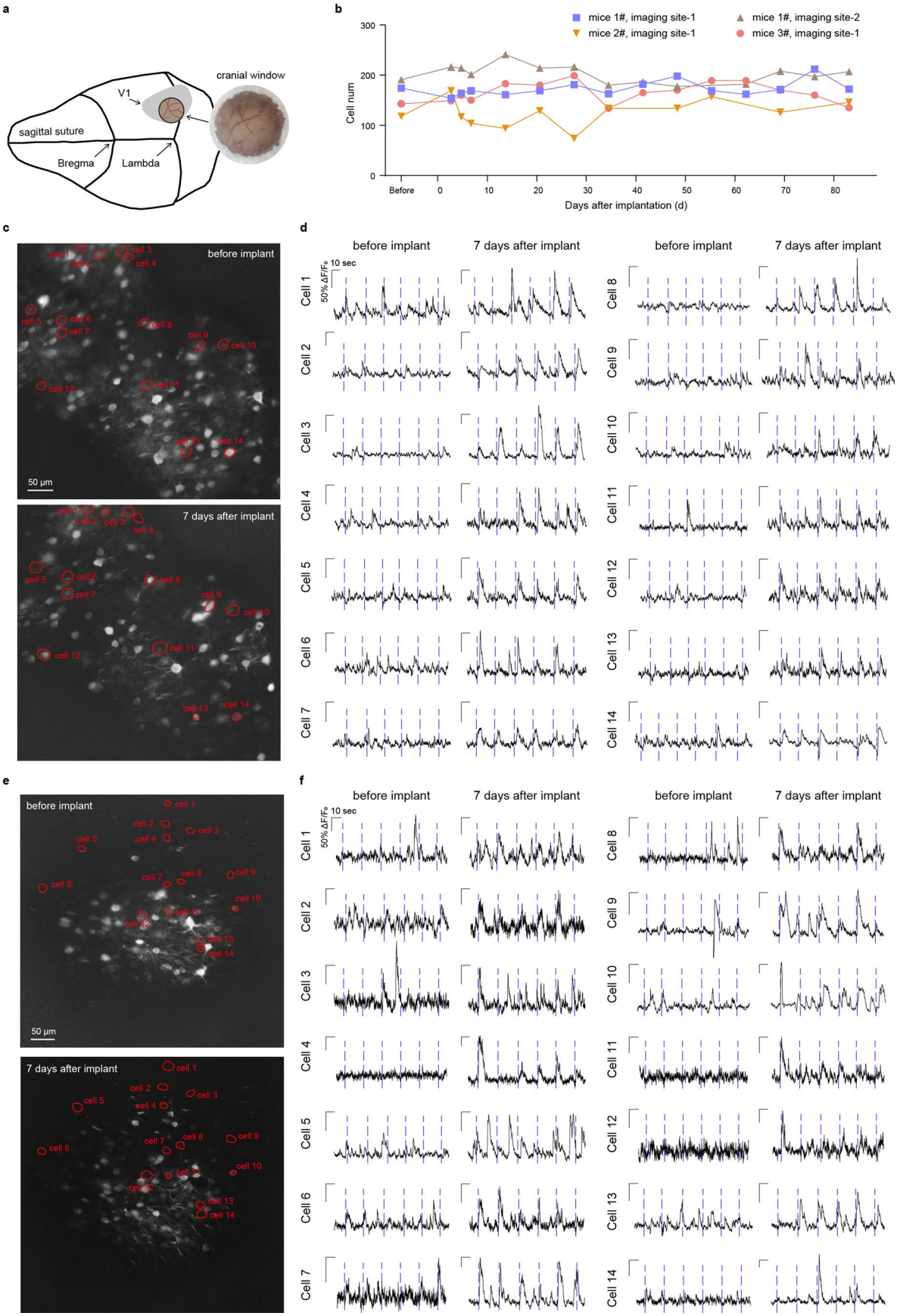

Extended Data Fig. 6 | See next page for caption.

https://doi.org/10.1038/s41551-023-01137-8

Extended Data Fig. 6 | Long-term light-evoked responses using two-photon calcium imaging in V1 of NW-array-implanted blind mice *in vivo*. **a**, Schematic of the position of the cranial window in V1 and the close-up of a completed cranial window by the day of surgery. **b**, The number of neurons in imaging site (n = 4 sites from 3 mice) recorded at different time points throughout the experiment. **c**,**e**, Grayscale images of recording fields of two blind mice before implantation (**c**) and 7 days after implantation (**e**). 14 representative light-responsive neurons were marked by red contours. Scale bars, 50 μm. **d**,**f**, The fluorescence changes of neurons in **c** and **e** in response to visual stimulations (Blue LED, 465/25 nm, 6.75 $\mu W \cdot mm^{-2}$, duration: 1 second). Dashed blue lines indicate the onset time of the visual stimulations.

https://doi.org/10.1038/s41551-023-01137-8

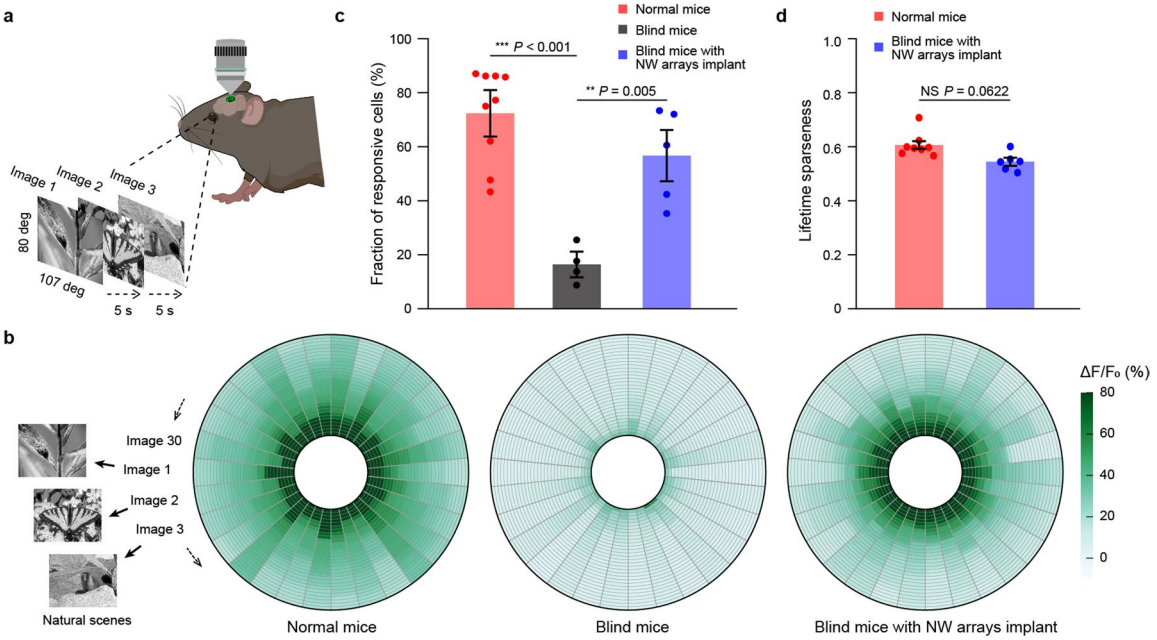

Extended Data Fig. 7 | Responses to natural scenes in V1 neurons of NW-array-implanted blind mice. a, Schematics of two-photon calcium imaging with natural scenes, which were presented for 0.5 sec followed by 5 sec inter-image gray periods. **b**, Examples of natural scenes and heatmaps of cellular responses to the natural scenes in normal mice (left, n = 3 mice), blind mice (middle, n = 4 mice) and blind mice with NW arrays implant (right, n = 4 mice). Each axial column represented responses of 30 neurons to one natural scene, with the strongest response positioned at the core. **c**, Fraction of neurons that responded to at least one natural scene in normal mice (72.36%, n = 3 mice), blind mice (16.69%, n = 4 mice) and blind mice with NW arrays implant (56.71%, n = 4 mice). **d**, Average lifetime sparseness of neurons in normal mice (0.61, n = 3 mice) and blind mice with NW arrays implant (0.54, n = 4 mice). All data are expressed as mean ± SEM. Statistical significance was determined using one-way ANOVA with Tukey's multiple comparisons in **c**, two-sided unpaired t-test in **d**. NS non-significant, * $P < 0.05$, ** $P < 0.01$.

https://doi.org/10.1038/s41551-023-01137-8

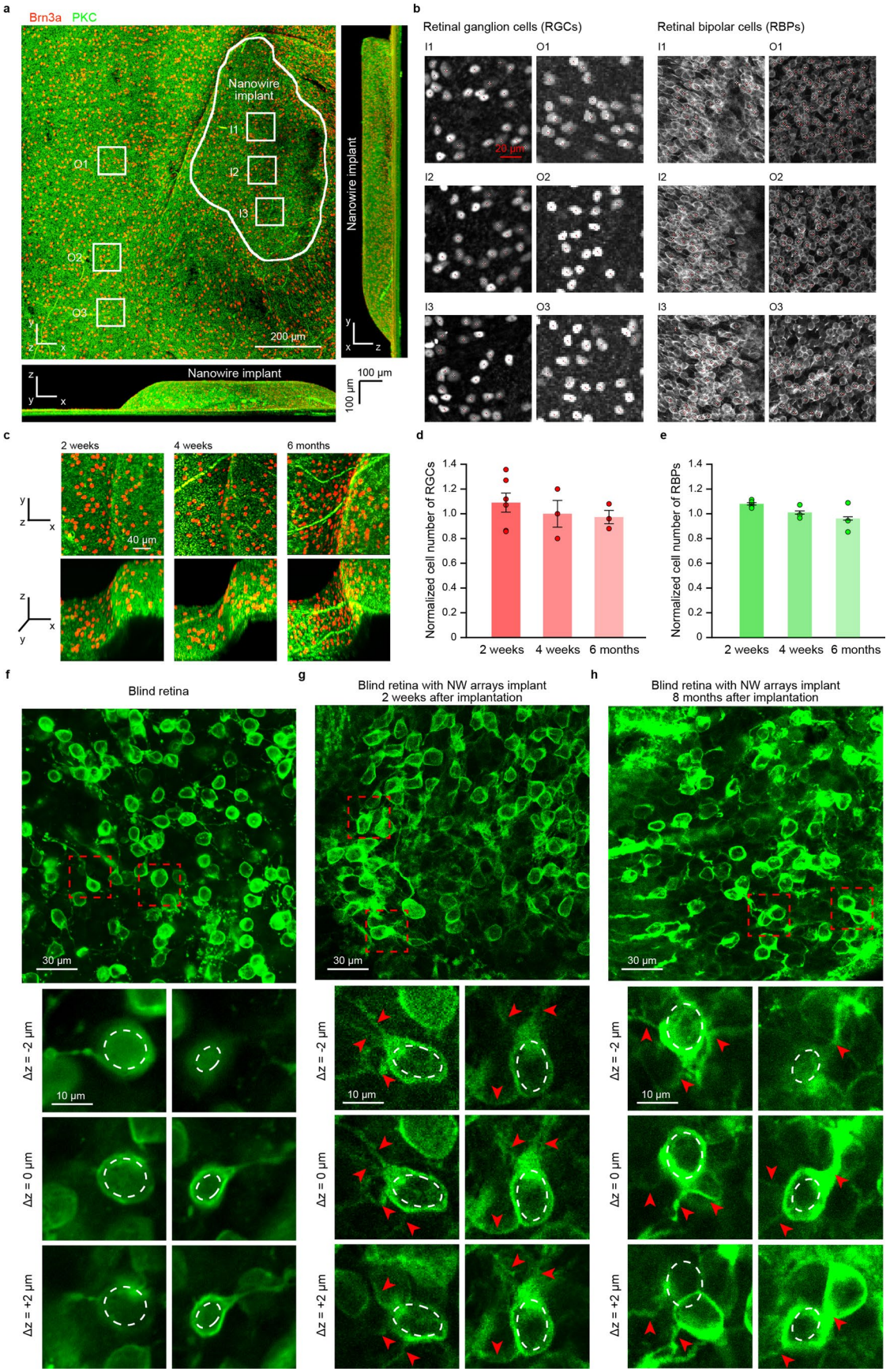

Extended Data Fig. 8 | See next page for caption.

https://doi.org/10.1038/s41551-023-01137-8

Extended Data Fig. 8 | Biocompatibility and dendritic structural analysis of implants in mice. a, A three-view diagram showing the 3-D outline of an implanted region and ROIs chosen for quantitative analysis. The shape of the NW arrays was represented by the convex of retina since it didn't emit detectable fluorescence signals. I: Interface, O: Outskirts. **b**, Example slices of z-stack images cropped by the ROIs in **a**, cross-dot markers illustrating identification of cells in these slices from corresponding fluorescence signals. Scale bar, 20 μm. **c**, 3-D reconstructed models of retinas at the borders of the NW arrays at 3 timepoints. Models were presented in x-y view (upper row) and x-z view with y axis rotated for 40 degrees towards z axis (lower row). The dark areas on the lower right side of the models were the edges of NW arrays. Scale bar, 40 μm. **d**,**e**, Quantitative analysis of RGC numbers (**d**) and RBP numbers (**e**) at 3 timepoints (n = 5 sites for 2 weeks, n = 3 sites for 4 weeks and 6 months). Cell numbers of RGCs and RBPs in each ROI at the interface were normalized to the average cell numbers of RGCs and RBPs of all ROIs at outskirt regions, respectively. **f**, Typical late-stage RP affected RBP structure from the intact eye of an implanted mouse. The mouse was implanted with NW arrays in another eye at P60 and was 10 months old upon perfusion. The upper graph showed the locations of two 30 μm × 30 μm ROIs (marked by red dashed squares) in a 200 μm × 200 μm window, generated by the maximum intensity projection of three consecutive slices in a z-stack. Two rows of zoomed-in ROIs showed the dendritic features of RBPs (marked by white dashed circles) in blind mice. Z-distances between two consecutive slices were 2 μm. Scale bars, 30 μm for top panels, 10 μm for bottom panels. **g**,**h**, Dendritic structures of interface RBPs from the retina of implanted eyes after 2 weeks (**g**) and 8 months (**h**). Subfigures were aligned as in **f**. Red arrows indicated the dendritic bifurcations. Scale bars, 30 μm for top panels, 10 μm for bottom panels. The experiments in **a**, **b**, **c**, **f** and **g** were carried out at least three times. The experiments in **h** were carried out two times. All data are expressed as mean ± SEM.

https://doi.org/10.1038/s41551-023-01137-8

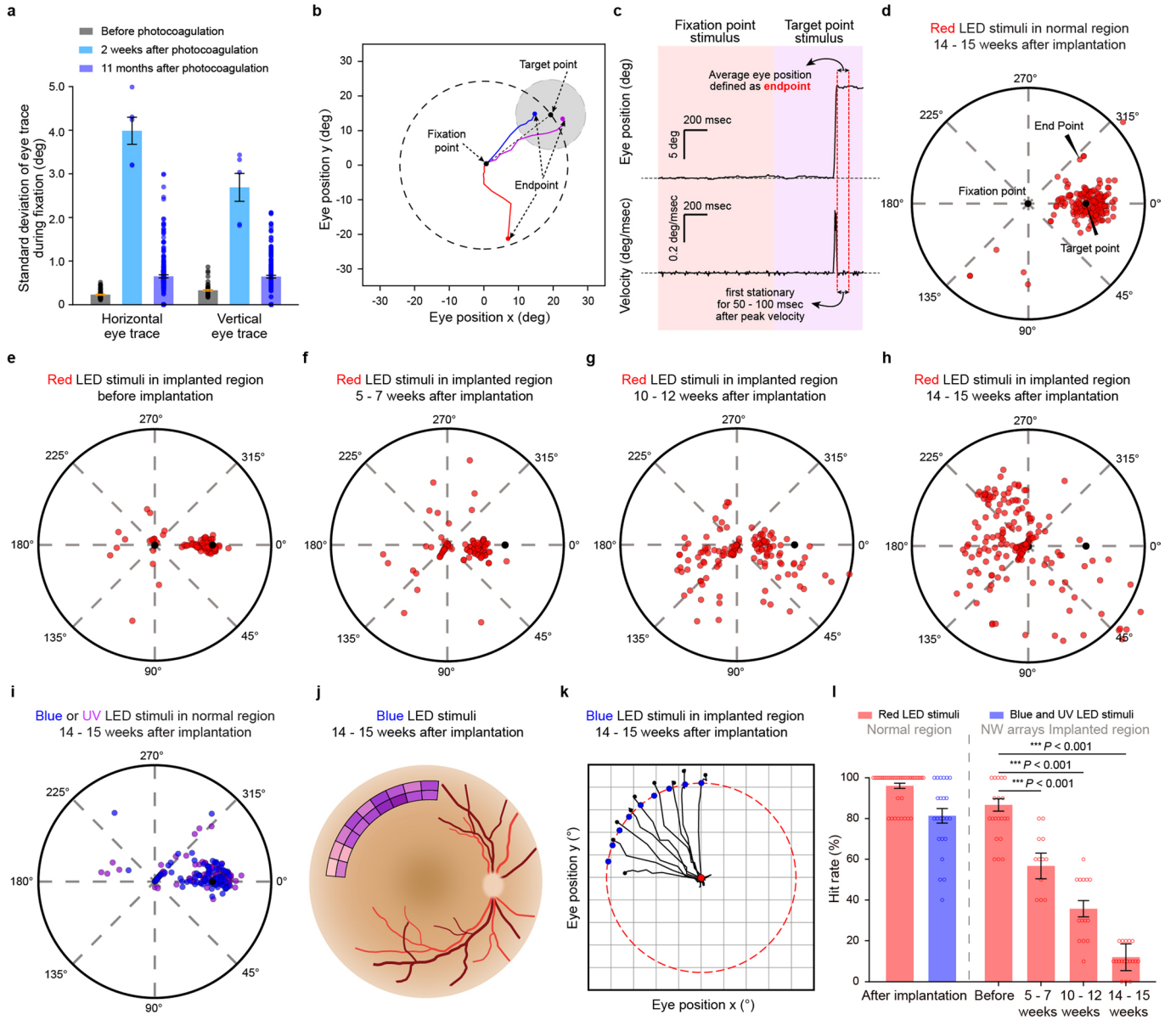

Extended Data Fig. 9 | VGS performance in Monkey A. a, Standard deviation of Monkey A's horizontal and vertical eye traces during fixation before photocoagulation (n = 64 trials), 2 weeks (n = 5 trials) and 11 months (n = 218 trials) after photocoagulation. **b**, Schematic of VGS task. The gray area indicates target area. **c**, Example traces of eye position and velocity in the VGS task. Dashed black lines indicate value of 0. **d**, Distribution of normalized saccadic endpoints in normal retinal regions (eccentricities: 19 and 21 degrees, polar angles: 40, 50 and 130 degrees) with red LED (642/18 nm) stimulus. **e**-**h**, Distribution of normalized saccadic endpoints using red LED in NW-array-implanted region (eccentricities: 19 and 21 degrees, polar angles: 200–250 degrees) before implantation, 5–7 weeks, 10–12 weeks and 14–15 weeks after implantation. **i**, Distribution of normalized saccadic endpoints in normal retinal regions (eccentricities: 19 and 21 degrees, polar angles: 40, 50 and 130 degrees) with blue (465/25 nm) and UV (360/15 nm) LED stimulus. **j**, Illustration of mean hit rates in VGS task of Monkey A with blue LED stimuli (0.5°, polar angle: 190 to 270 degrees, eccentricity: 19 and 21 degrees) 14–15 weeks after implantation. **k**, Example saccadic trace of Monkey A in response to blue stimuli in the target points (polar angle: 190 to 270 degrees, eccentricity: 21 degrees), corresponding to **j**. **l**, Mean hit rates of VGS task in **d**-**i**. Normal region: n = 40 sessions for Red LED stimuli, n = 23 sessions for Blue LED stimuli. NW arrays implanted region: n = 20 sessions for Before, n = 12 sessions for 5–7 weeks, n = 14 sessions for 10–12 weeks, n = 18 sessions for 14–15 weeks. All data are expressed as mean ± SEM. Statistical significance was determined using one-way ANOVA with Tukey's multiple comparisons in **l**. *** $P < 0.001$.

https://doi.org/10.1038/s41551-023-01137-8

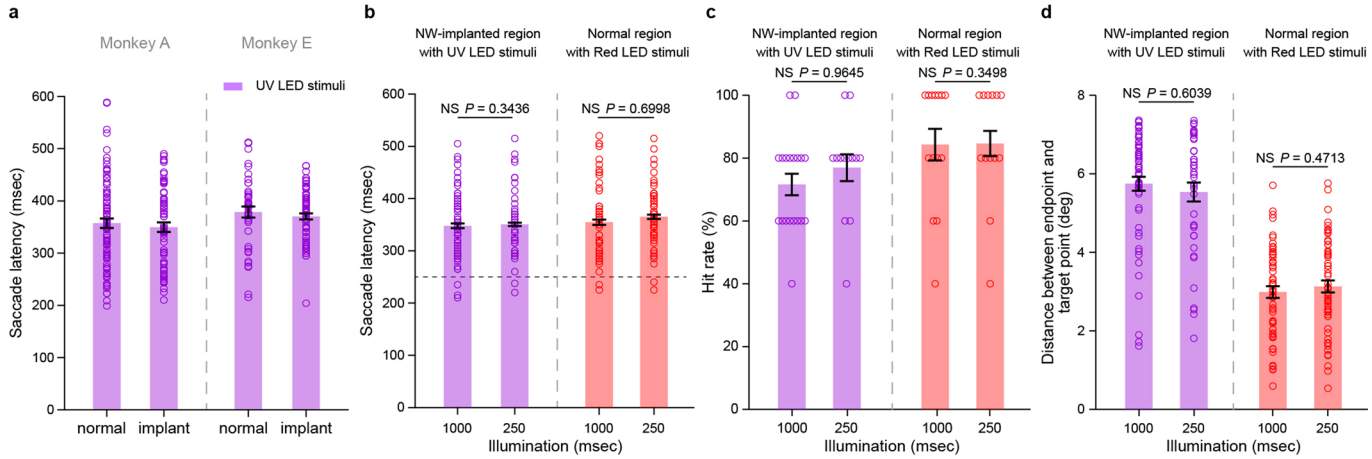

Extended Data Fig. 10 | Saccade latency, hit rate and distance between saccadic endpoint and target point in VGS task. a, Saccade latency of monkey A (left) and E (right). Left: saccade latency of monkey A to UV LED stimuli in normal regions and NW arrays implanted regions at 14–15 weeks after implantation. Right: saccade latency of monkey E to UV LED stimuli in normal regions and NW arrays implanted regions at 18–20 weeks after implantation. Monkey A: normal, n = 285 trials, implant, n = 68 trials, Monkey E: normal, n = 44 trials, implant, n = 72 trials. **b**, Saccade latency for 1000 msec and 250 msec illuminations with UV LED stimuli in NW-array-implanted region (left) and red LED stimuli in normal region (right). UV LED stimuli: 360/15 nm, 10.00 μW·mm^{-2}. Red LED stimuli: 642/18 nm, 10.00 μW·mm^{-2}. NW-array-implanted region: 1000 msec, n = 60 trials; 250 msec, n = 60 trials. Normal region: 1000 msec, n = 60 trials; 250 msec, n = 40 trials. Dashed black line indicates 250 msec of saccade latency. **c**, Hit rate for 1000 msec and 250 msec illuminations with UV LED stimuli in NW-array-implanted region (left) and red LED stimuli in normal region (right). NW-array-implanted region: 1000 msec, n = 19 sessions; 250 msec, n = 13 sessions. Normal region: 1000 msec, n = 14 sessions; 250 msec, n = 13 sessions. **d**, Distance between saccadic endpoint and target point for 1000 msec and 250 msec illuminations with UV LED stimuli in NW-array-implanted region (left) and red LED stimuli in normal region (right). NW-array-implanted region: 1000 msec, n = 60 trials; 250 msec, n = 60 trials. Normal region: 1000 msec, n = 60 trials; 250 msec, n = 40 trials. All data are expressed as mean ± SEM. Statistical significance was determined using two-sided unpaired t-test in **b**, **c** and **d**. NS non-significant.

nature portfolio

Corresponding author(s): Jiayi Zhang, Biao Yan, Yuanzhi Yuan, Chunhui Jiang

Last updated by author(s): Oct 10, 2023

Reporting Summary

Nature Portfolio wishes to improve the reproducibility of the work that we publish. This form provides structure for consistency and transparency in reporting. For further information on Nature Portfolio policies, see our Editorial Policies and the Editorial Policy Checklist.

Statistics

For all statistical analyses, confirm that the following items are present in the figure legend, table legend, main text, or Methods section.

n/a	Confirmed	
☐	☒	The exact sample size (*n*) for each experimental group/condition, given as a discrete number and unit of measurement
☐	☒	A statement on whether measurements were taken from distinct samples or whether the same sample was measured repeatedly
☐	☒	The statistical test(s) used AND whether they are one- or two-sided *Only common tests should be described solely by name; describe more complex techniques in the Methods section.*
☒	☐	A description of all covariates tested
☐	☒	A description of any assumptions or corrections, such as tests of normality and adjustment for multiple comparisons
☐	☒	A full description of the statistical parameters including central tendency (e.g. means) or other basic estimates (e.g. regression coefficient) AND variation (e.g. standard deviation) or associated estimates of uncertainty (e.g. confidence intervals)
☐	☒	For null hypothesis testing, the test statistic (e.g. *F*, *t*, *r*) with confidence intervals, effect sizes, degrees of freedom and *P* value noted *Give P values as exact values whenever suitable.*
☒	☐	For Bayesian analysis, information on the choice of priors and Markov chain Monte Carlo settings
☒	☐	For hierarchical and complex designs, identification of the appropriate level for tests and full reporting of outcomes
☒	☐	Estimates of effect sizes (e.g. Cohen's *d*, Pearson's *r*), indicating how they were calculated

Our web collection on statistics for biologists contains articles on many of the points above.

Software and code

Policy information about availability of computer code

Data collection	In the in vitro patch clamp experiments, data were collected by Clampex 10.5. In choice-box behavioural experiments, visual stimulus was controlled by Arduino and Psychopy3. In in vivo two-photon calcium imaging, data were collected by MAITAI eHPDS-OL laser with an Olympus XL Plan N25 × /1.05 WMP ∞/0-0.23/FN/19 dipping objective (Olympus, Tokyo, Japan) and a miniature two-photon microscope (DPHLMTPM-V2.0, Beijing Transcend Vivoscope Biotech Co. Ltd., China). In visually-guided saccade task, visual stimulus was controlled by Arduino and Neurontask software (0.3-pre alpha, SourceForge, San Diego, USA) and data were collected by Tempo experiment control system (Reflective computing, Olympia, WA, USA). In VEP recording experiments, all extracellular signals were amplified (×200) and sampled (20 kHz) using a multichannel data-acquisition system (Bio-signal Technologies, China).
Data analysis	In vitro patch-clamp experiments: CED spike2 v7.16, Python 3.7. In vivo VEP-recording experiments: CED spike2 v7.16, Plexon offline sorter v3.3.5, Python 3.7. In vivo two-photon calcium-imaging data analysis: CaImAn v1.9, Python 3.7. Behavioural experiments: MATLAB R2020a, Python 3.7. Statistic analysis: SigmaPlot v12.5, Prism v9.5.

For manuscripts utilizing custom algorithms or software that are central to the research but not yet described in published literature, software must be made available to editors and reviewers. We strongly encourage code deposition in a community repository (e.g. GitHub). See the Nature Portfolio guidelines for submitting code & software for further information.

Data

Policy information about availability of data

All manuscripts must include a data availability statement. This statement should provide the following information, where applicable:

- Accession codes, unique identifiers, or web links for publicly available datasets
- A description of any restrictions on data availability
- For clinical datasets or third party data, please ensure that the statement adheres to our policy

The raw and analysed datasets generated during the study are available for research purposes from the corresponding authors on reasonable request. Source data for the figures are provided with this paper. The study using stimuli of natural scenes used 30 natural images from the van Hateren Natural Image Dataset (https://github.com/hunse/vanhateren) and the McGill Calibrated Colour Image Database (http://tabby.vision.mcgill.ca.).

Field-specific reporting

Please select the one below that is the best fit for your research. If you are not sure, read the appropriate sections before making your selection.

☒ Life sciences ☐ Behavioural & social sciences ☐ Ecological, evolutionary & environmental sciences

For a reference copy of the document with all sections, see nature.com/documents/nr-reporting-summary-flat.pdf

Life sciences study design

All studies must disclose on these points even when the disclosure is negative.

Sample size	Required sample sizes were estimated on the basis of published results and of our past experience performing similar experiments. No statistical methods were used to predetermine sample sizes, but our sample sizes are similar to those reported in previous publications (n = 2–12 mice in Y. Lu, Nature, 588, 124-129 (2020); n = 3–6 mice in B. Mahato, Nature, 581, 83-88 (2020); n = 3–8 mice in our study. n = 2 macaque monkeys in X. Chen, Science, 370, 1191-1196 (2020); n = 2 macaque monkeys in our study). The sample size for each experiment is provided in the corresponding figure captions.
Data exclusions	No data were excluded from the analyses.
Replication	Animal experiments were performed on biological replicates following identical procedures to verify the reproducibility of the experimental findings in six months, and all attempts at replication were successful. Animal behavioural experiments, in vivo electrophysiological experiments, immunohistochemistry and patch-clamp experiments were repeated at least with 3 independent biological repeats.
Randomization	The mice used in the experiments were randomly allocated into the positive and control groups. Visual stimuli in the behavioural experiments were presented randomly.
Blinding	All data were collected and assembled by instrument software without interference. The investigators were not blinded to group allocation during data collection, because it is necessary to record information for the groups as a proper experiment documentation. The investigators were blinded to data analysis instead.

Reporting for specific materials, systems and methods

We require information from authors about some types of materials, experimental systems and methods used in many studies. Here, indicate whether each material, system or method listed is relevant to your study. If you are not sure if a list item applies to your research, read the appropriate section before selecting a response.

Materials & experimental systems

n/a	Involved in the study
☐	☒ Antibodies
☒	☐ Eukaryotic cell lines
☒	☐ Palaeontology and archaeology
☐	☒ Animals and other organisms
☒	☐ Human research participants
☒	☐ Clinical data
☒	☐ Dual use research of concern

Methods

n/a	Involved in the study
☒	☐ ChIP-seq
☒	☐ Flow cytometry
☒	☐ MRI-based neuroimaging

Antibodies

Antibodies used	1. Anti-Brn3a antibody, Cat# sc-31984, 1:200, Santa Cruz, US. 2. Anti-PKC alpha antibody, Cat# MA1-157, 1:200, Thermo Fisher, US.

3. Anti-ATP1A3 antibody, Cat# ab182571, 1:200, Abcam, UK.
4. Anti-S Opsin antibody, Cat# ab235274, 1:200, Abcam, UK.
5. Donkey anti goat 488 secondary antibody, Cat# 705-547-003, 1:300, Jackson ImmunoResearch, US.
6. Donkey anti goat 594 secondary antibody, Cat# 705-585-003, 1:300, Jackson ImmunoResearch, US.
7. Donkey anti rabbit 594 secondary antibody, Cat# 711-585-152, 1:300, Jackson ImmunoResearch, US.
8. Donkey anti mouse 488 secondary antibody, Cat# 715-545-150, 1:300, Jackson ImmunoResearch, US.
9. Donkey anti mouse 647 secondary antibody, Cat# 715-605-150, 1:300, Jackson ImmunoResearch, US.

Validation

Validation details of the primary antibodies are available on the manufacturers' websites and in these related references:
1. Brn3a, Cat# sc-31984, https://www.scbt.com/p/brn-3a-antibody-c-20?requestFrom=search, Trost A et al. (pubmed id: 26001526)
2. PKC alpha, Cat# MA1-157, https://www.thermofisher.cn/cn/zh/antibody/product/PKC-alpha-Antibody-clone-MC5-Monoclonal/MA1-157, Maddox JW et al. (pubmed id: 32940604)
3. ATP1A3, Cat# ab182571, https://www.abcam.cn/atp1a3-antibody-epr14138-ab182571.html, Fernández ÁF, et al. (pubmed id: 31941841)
4. S Opsin, Cat# ab235274, https://www.abcam.com/products/primary-antibodies/s-opsinbcp-antibody-ab235274.html

Animals and other organisms

Policy information about studies involving animals; ARRIVE guidelines recommended for reporting animal research

Laboratory animals

C57BL/6J mice were purchased from Shanghai Laboratory Animal Center, Chinese Academy of Sciences. rd1-/-/cDTA lines were kindly provided by Tian Xue at University of Science and Technology of China. With the exception of the behavioural experiments, which exclusively used male mice, the other experiments were conducted using mice of unspecified gender. Details about age are provided in Results and in Supplementary Table 1.

Two male rhesus monkeys (Macaca mulatta, 12 years old, 8-13 kg) were purchased from ZHONGKE (Suzhou Xishan Zhongke Laboratory Animal Co., Ltd.) and raised in Primate Center at East China Normal University.

Wild animals

The study did not involve wild animals.

Field-collected samples

The study did not involve samples collected from the field.

Ethics oversight

All protocols for the mouse experiments were approved by the Animal Ethics Committee of School of Basic Medical Sciences at Fudan University. Rhesus monkey surgical and experimental procedures were approved by the Institutional Animal Care and Use Committee at East China Normal University (Protocol number: Mo20200101).

Note that full information on the approval of the study protocol must also be provided in the manuscript.